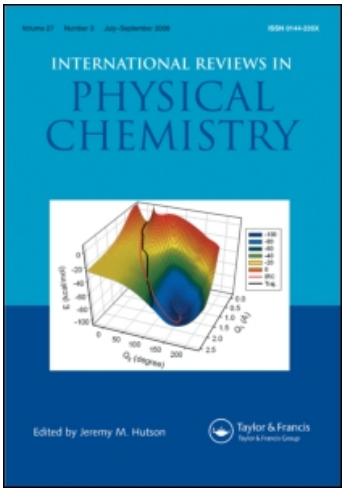

International Reviews in Physical Chemistry
Publication details, including instructions for authors and subscription information:
http://www.informaworld.com/smpp/title~content=t713724383

Structural studies on transition metal compounds

Yoshihiko Saito[a]
[a] Keio University, Yokohama, Japan

To cite this Article Saito, Yoshihiko(1989) 'Structural studies on transition metal compounds', International Reviews in Physical Chemistry, 8: 2, 235 — 273
To link to this Article: DOI: 10.1080/01442358909353230
URL: http://dx.doi.org/10.1080/01442358909353230

INTERNATIONAL REVIEWS IN PHYSICAL CHEMISTRY, 1989, VOL. 8, NOS. 2/3, 235–273

Structural studies on transition metal compounds

by YOSHIHIKO SAITO
Keio University, Kohoku-ku, Yokohama 223, Japan

Accurate determination of the electron-density distribution in transition metal complexes provides important information on the electronic ground state of the d electrons placed in a ligand field. The high-spin and low-spin states can be distinguished unequivocally. The degree of hybridization of the component orbitals can also be determined. If the intensity data are good enough, the wavefunction analysis can be carried out and the orbital coefficients can be obtained by a least squares method. In spite of a very small valence/total electron ratio the asphericity of 4d and 5d electrons in a ligand field can be detected. This is owing to sharp deformation density located outside of the high-density inner core region.

The crystal structures of a series of dimeric copper(II) carboxylate adducts of the general formula $[Cu(RCOO)_2L]_2$ have been accurately determined or redetermined. The temperature-dependent magnetic susceptibility of these crystals indicates that the isolated pairs of Cu(II) ions interact strongly through exchange forces. The present structure investigation has established that there exist no magneto-structural correlations. Instead, it was found that the values of singlet–triplet separation increase roughly linearly with the number of electrons in the bridging OCO group calculated by the molecular orbital method.

The chiral cyanoethyl group in a series of cobaloxime complexes was found to racemize on exposure to X-rays without degradation of crystallinity. The rate of racemization was so slow that several structures of intermediate stages could be determined by X-ray analysis. In this way various reaction pathways were recognized and the reaction rate could be correlated quantitatively with the atomic arrangement in the crystal. The related complexes were found to undergo reversible phase transition and/or photoisomerization without degradation of crystallinity.

1. Introduction

Three quarters of a century has passed since Laue's discovery of X-ray diffraction in 1912. Since that time advances in experimental and theoretical diffraction crystallography have been considerable. At an early stage of the development, X-ray crystal structure analysis mainly aimed at the determination of the atomic positions, that is, the elucidation of the geometrical structure of a molecule. Nowadays, however, the advent of automated four-circle diffractometers combined with the development of electronic computers has made it possible to measure accurately the electron-density distribution around the atomic nuclei. Knowledge of electron-density distribution in a molecule provides deeper insight into the question of what happens when an atom unites with another atom to form a molecule. Also, the amount of time needed to solve any particular structure could be significantly shortened. At present, structures of coordination compounds of moderate complexity can be solved in one or two days. During the period from 1935 to 1969 about 4500 structures were reported. At present, about the same number of structures are solved in one year and the number is still increasing year by year. In this way it is now easy to compare and discuss a number of related structures at one time. X-ray crystal structure determination is no more in the hands of a limited number of crystallographers but it is now an indispensable tool for chemists in general. In this paper an overview will be given on the structural studies of

0144-235X/89 $3·00

transition metal compounds. It is not intended to be a complete review but to select relevant topics and show some distinctive features of the recent activity in physical chemistry of solids in this country.

2. Electron-density distributions determined by X-ray diffraction methods

When the incident beam of X-rays passes over the atoms in a crystal, each atom scatters the incident X-rays. Owing to the periodic arrangement of atoms constructive interference between scattered wavelets takes place to give diffracted beams. The scattering amplitudes depend directly on the electron-density distribution in a crystal, from which atomic positions can be derived on the assumption of coincidence of the nuclear positions and the 'centres of gravity' of total electron densities around atomic nuclei. The scattering amplitude from one unit cell is given by the absolute value of a Fourier transform of the total electron-density distribution in a unit cell:

$$F(\mathbf{H}) = \int_{\text{unit cell}} \rho(\mathbf{r}) \exp(2\pi i \mathbf{H} \cdot \mathbf{r}) \, d\tau, \tag{1}$$

where $\mathbf{r}$ is a position vector in real space and $\mathbf{H}$ is a reciprocal lattice vector. $F(\mathbf{H})$ is called the structure factor. Equation (1) can be reformed into a summation of the contributions from each atom in the unit cell as follows:

$$F(\mathbf{H}) = \sum_{\substack{\text{unit} \\ \text{cell}}} f_j T_j \exp(2\pi i \mathbf{H} \cdot \mathbf{r}_j), \tag{2}$$

where $\mathbf{r}_j$ represents the atomic position of the jth atom and f_j is the Fourier transform of the atomic electron-density centred at the nuclear position of the jth atom and T_j is the temperature factor that incorporates the effect of thermal vibration of the atom. f_j is called the atomic scattering factor.

The electron-density $\rho(\mathbf{r})$ at position $\mathbf{r}$ in the unit cell is given by the inverse Fourier transform,

$$\rho(\mathbf{r}) = \frac{1}{v} \sum_{\mathbf{H}} |F(\mathbf{H})| \exp(2\pi i \mathbf{H} \cdot \mathbf{r} - i\alpha_{\mathbf{H}}), \tag{3}$$

where V is the volume of the unit cell and summation is taken over all the reciprocal lattice points. $F(\mathbf{H})$ is generally a complex quantity the absolute value (structure amplitude) of which can be obtained from the measured intensity of X-ray diffraction, however, its phase angle $\alpha_{\mathbf{H}}$ cannot be measured directly. The value of $\alpha_{\mathbf{H}}$ are calculated after the crystal structure has been completely determined. At the beginning of the crystal structure analysis, the approximate values of the phase angles can be deduced based on intensity statistics, Patterson synthesis and other clues. The electron-density distribution $\rho(\mathbf{r})$ is calculated with the observed structure amplitudes combined with the phase angles, from which approximate atomic coordinates are derived. The structure amplitudes are calculated in terms of the atomic coordinates and compared with the observed values. The atomic coordinates are then adjusted to obtain better agreement between the observed and calculated structure amplitudes by successive approximations. At the final stage, the atomic coordinates are refined by the least-squares method. The estimate of agreement between the observed and calculated structure amplitudes is assessed by an R factor:

$$R = \frac{\sum \| F_o(\mathbf{H}) | - | F_c(\mathbf{H}) \|}{\sum_{\mathbf{H}} |F_o(\mathbf{H})|}, \tag{4}$$

where $|F_o(\mathbf{H})|$ and $|F_c(\mathbf{H})|$ are the observed and calculated structure amplitudes. Most of the refined structures have R values less than 0·070.

Valence electron-density, containing chemically important information, is relatively small compared to the total electron-density in magnitude. Thus a more sensitive function must be introduced to examine the changes undergone in a process of bond formation. One of such functions is the deformation density. This is the difference between the total electron-density and the pro-molecule density, where the pro-molecule density is the electron-density prior to the formation of bonds (i.e. the superposition of spherical free-atom densities each centred at its position in the molecule). The pro-molecule density can be calculated from equations (2) and (3), using spherical atomic scattering factors for f_j.

$$\delta\rho(\mathbf{r}) = \rho(\mathbf{r}) - \rho(\mathbf{r})_{\text{pro-molecule}}. \tag{5}$$

Deformation density represents the rearrangement of the electron-density due to interatomic bonding. Generally the difference between the observed and calculated electron-density is called difference density, which is familiar to X-ray crystallographers.

When atoms form chemical bonds, the valence shell will expand or contract with variation of atomic charge and valence density becomes aspherical. Such behaviour of the valence density can be analysed by least-squares refinement on the basis of observed structure amplitudes. The atomic scattering factor f_j in equation (2) is rewritten as a sum of contributions of core and valence electrons (Dawson 1967, Stewart 1969, Hirshfeld 1977).

$$f_j = f_{j\,\text{core}} + P_{j\,\text{valence}} f_{j\,\text{valence}} + \sum_l \sum_m P_{jlm} f_{jlm}. \tag{6}$$

The second and third terms are the Fourier transforms of the spherical and aspherical valence electron density respectively. $P_{j\,\text{valence}}$ and P_{jlm} are population parameters. The aspherical density fragments in real space are functionally identical to the p, d, f, g... hydrogen atom orbitals, where the angular functions are the well known spherical harmonics, which are labelled with the quantum numbers l and m, with values $l=1$, 2, 3, 4, 5... representing dipolar, quadrupolar, octopolar, hexadecapolar... functions. An important distinction is that this describes the probability distribution of electrons rather than the wavefunctions. A factor multiplying the radial coordinates of the atomic valence density, allowing expansion or contraction of the valence shell with variation of atomic charge is included in the second and third terms in equation (6). By using the expression for f_j given in equation (6) all the adjustable parameters on all atoms can be refined by the least-squares method on the basis of observed structure amplitudes (Hansen and Coppens 1978). This procedure is called multipole refinement. If the aspherical scattering factors obtained after the multipole refinement are used to calculate the electron density, the calculated electron density approaches gradually to the observed density as the refinement proceeds. Thus difference map will eventually becomes featureless, leaving random errors.

3. d-electron-density distribution

Since the aspherical distributions of the 3d electrons in crystals of $[Co(NH_3)_6][Co(CN)_6]$ were detected for the first time (Iwata and Saito 1973), a number of studies on transition metals and their complexes have been carried out (Coppens and Hall 1982, Toriumi and Saito 1983). On the other hand, theoretical

calculation was carried out for the asphericity of d electron charge density by using *ab initio* Hartree–Fock and configuration interaction methods (Johansen 1976). The calculated results coincide qualitatively with the experimental results, although the peaks are too high and too close to the centres of the atoms compared with the experiments.

3.1. *3d electron density*

A series of studies on electron-density distributions in crystals of perovskite type KMF_3(M = Fe, Co, Mn and Cu) have been performed. Crystals of KMF_3 except for M = Cu are cubic and K^+ ions are arranged at the apices of a cube. The M^{2+} ion lies at the cube centre and F^- ions are located at the centres of the cube faces, thus M^{2+} is surrounded octahedrally by six F^- ions. It was shown that a number of important items of information on the electronic ground state can be obtained by examining the asphericity of 3d electrons. The intensity data were collected at room temperature, unless otherwise stated. However, all the crystal specimens are 'hard' and the thermal vibration amplitudes are smaller than those of organic compounds. This situation enables the asphericity of 3d electrons to be detected successfully even at room temperatures.

3.1.1. $KCoF_3$ (*Kijima* et al. *1981*)

Figure 1 shows the deformation density around the Co^{2+} ion. Six large troughs of $-0{\cdot}83\ e\ Å^{-3}$ are located on the Co–F bonds at 0·47 Å from the Co nucleus. Eight small positive peaks are also observed at about 0·5 Å from the Co nucleus in the ⟨111⟩ directions, avoiding ligands. Such features are also observed in γ-Co_2SiO_4 (Marumo *et al.* 1977). The six negative peaks in the Co–F bonds in figure 1 indicate that the electron-density of the t_{2g} orbital is higher than that of the e_g orbital. However, from figure 1 alone it is difficult to decide whether the 3d electronic state of the Co^{2+} ions in $KCoF_3$ is in high spin or low spin. Even if the electronic state is low spin, qualitatively similar peaks would appear on the difference maps after the refinement with spherical scattering factors, because the electron population should also be higher in the t_{2g} orbital than in the e_g orbital in the low-spin state. Therefore quantitative analysis was carried out with aspherical scattering factors for the 3d electrons to distinguish the electronic state. Figure 2 is the difference map around the Co^{2+} ion calculated after the refinement with the high-spin model. Six large troughs around the Co nucleus in figure 1 completely disappear in figure 2 and new small positive peaks of $0{\cdot}49\ e\ Å^{-3}$ appear on the Co–F bonds at 0·24 Å from the Co nucleus. On the other hand, eight troughs of $-0{\cdot}32\ e\ Å^{-3}$ appear at 0·49 Å from the Co site on the lines along ⟨111⟩ in place of the eight positive peaks in figure 1. The residual densities in the region far from the Co^{2+} ion did not change significantly. Since the high-spin model improved the residual density maps and the R value was reduced from 0·0088 to 0·0077, it was confirmed that the real electronic state of the Co^{2+} ion is close to the high-spin state. However, this model does not represent exactly the real electronic state of the Co^{2+} ion, since new peaks emerge in figure 2. Namely, there seems to be fewer 3d electrons in the t_{2g} orbitals than in the ideal $(t_{2g})^5(e_g)^2$ state. The difference maps (figure 2) suggest that the electronic state is intermediate between $(t_{2g})^5(e_g)^2$ and $(t_{2g})^4(e_g)^3$. Consequently, a refinement in which x of $(t_{2g})^{5-x}(e_g)^{2+x}$ was treated as an unknown parameter, was performed to determine the population of the t_{2g} and e_g orbitals quantitatively. The R value reduced slightly from 0·0077 to 0·0076 and the value of x converged to 0·25 with

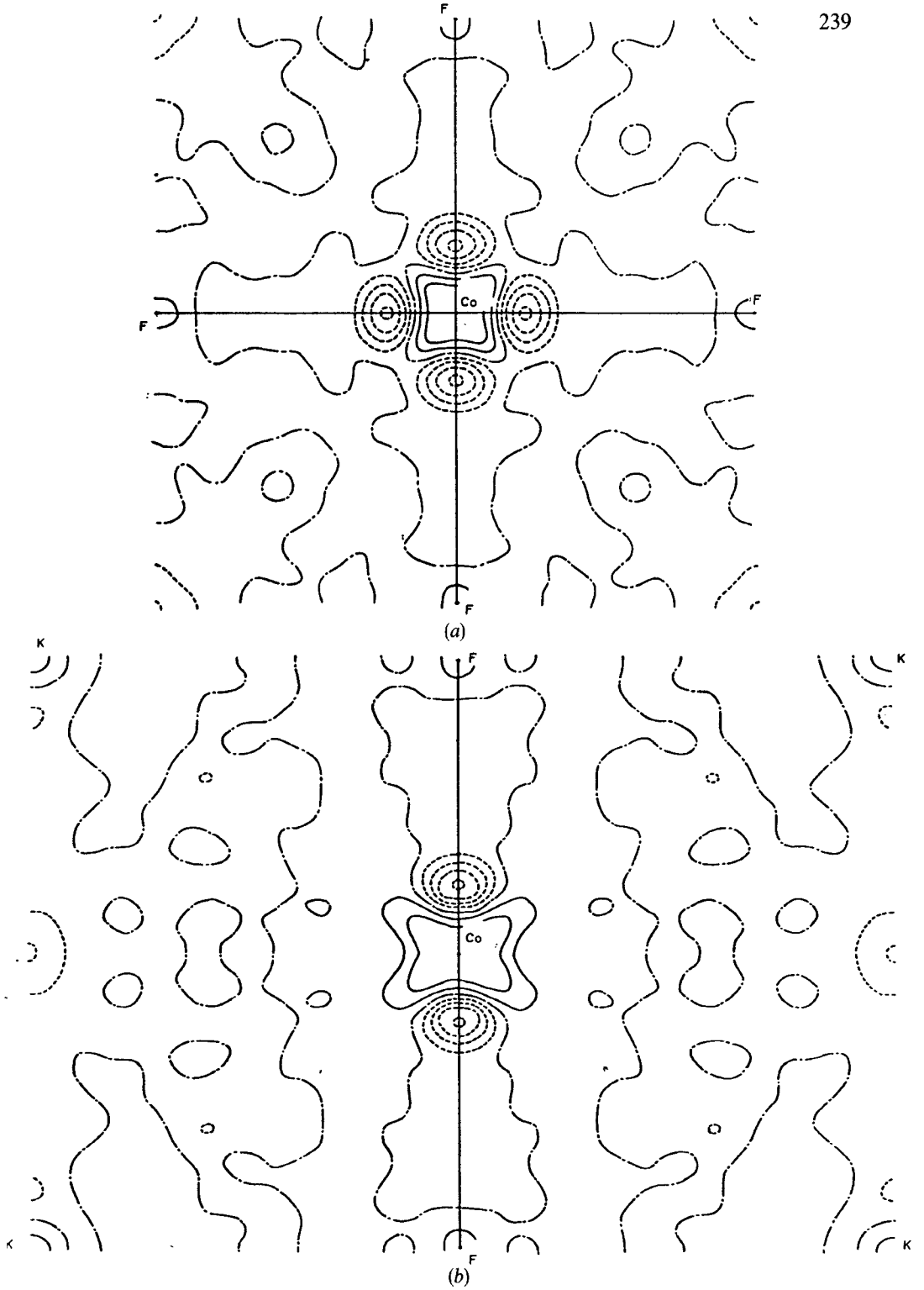

Figure 1. Sections of the deformation density of $KCoF_3$ after refinement with spherical scattering factors through the planes (*a*) $x = 0$ and (*b*) $y = x$. Contours are drawn at intervals of 0·2 e Å^{-3}. Negative (- - -) and zero (—·—) contours.

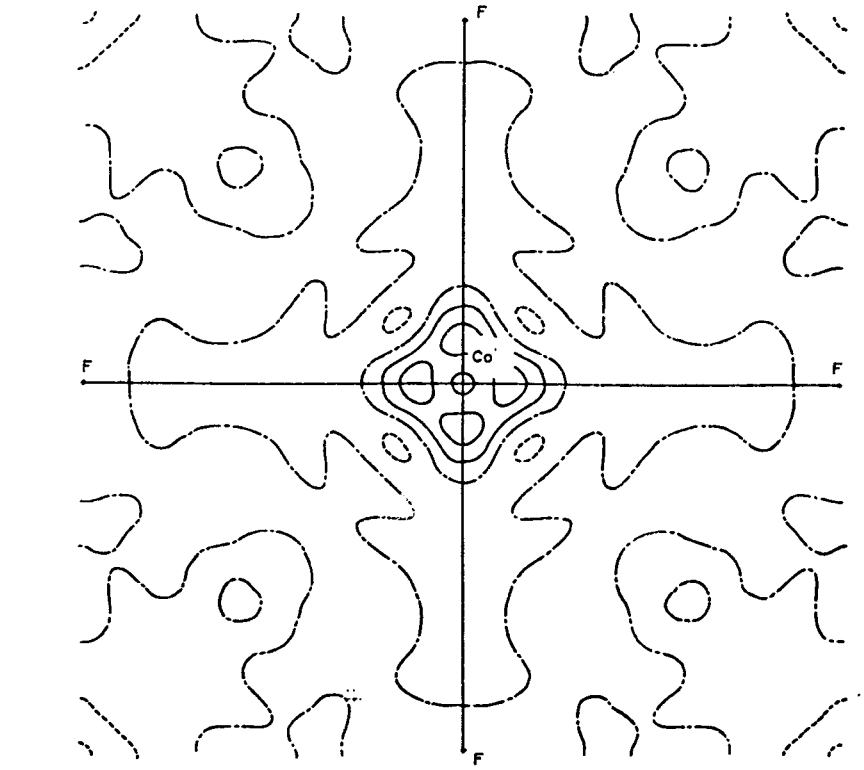

(*a*)

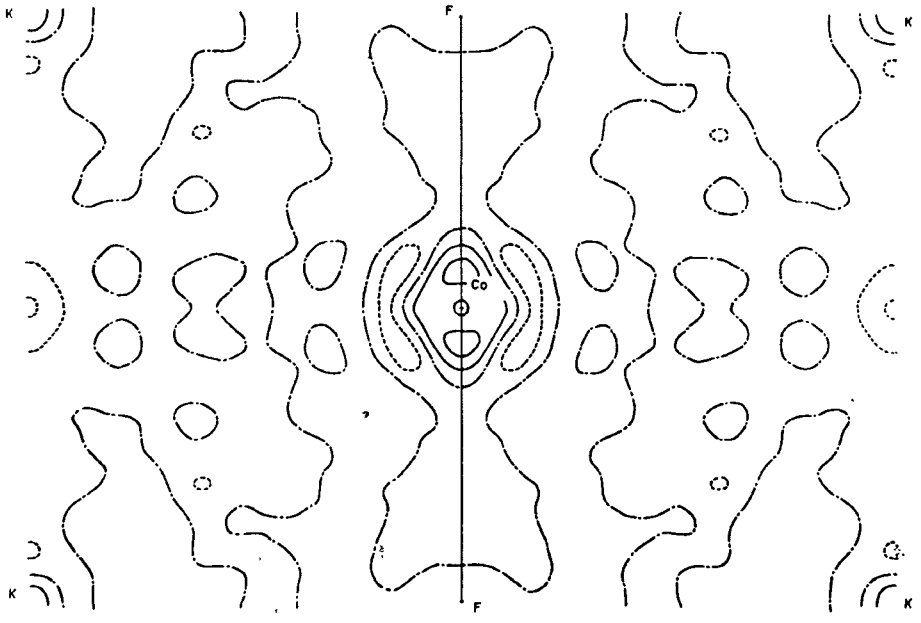

(*b*)

Figure 2. The same section of the difference density as those in figure 1. The maps are drawn in the same way as in figure 1.

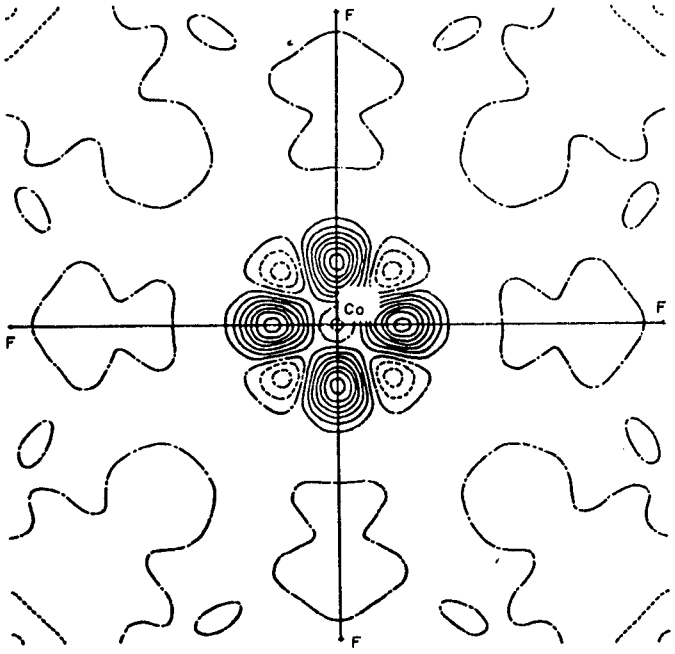

(*a*)

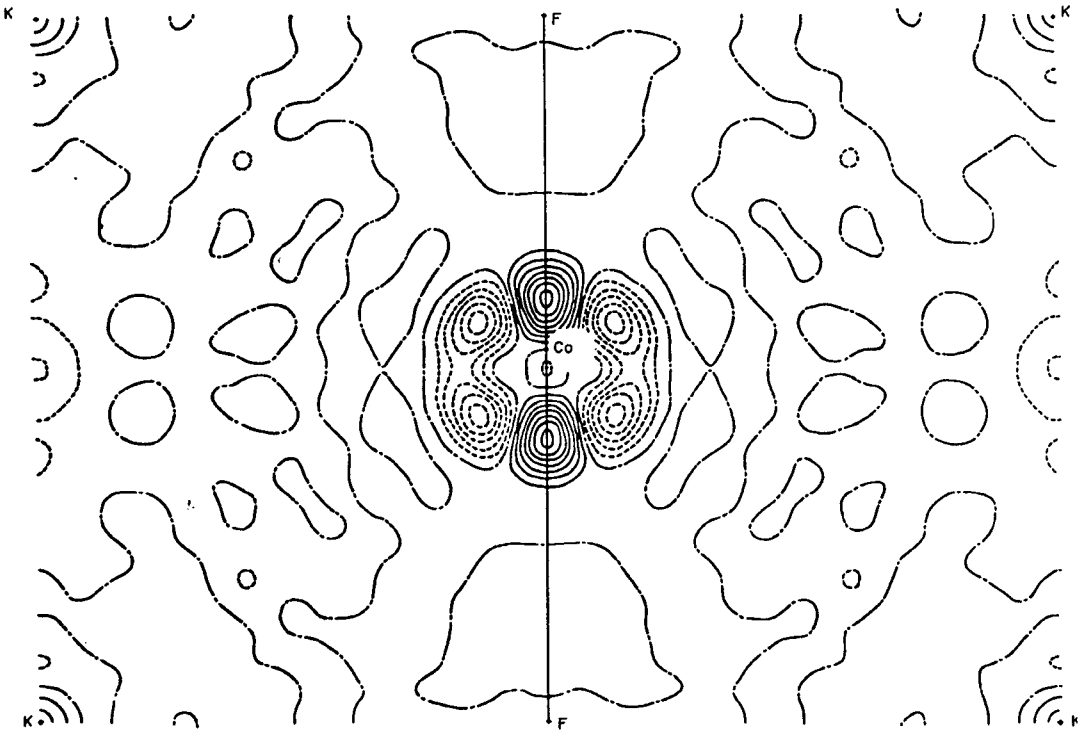

(*b*)

Figure 3. The difference maps after the refinement with the low-spin state assumed. Maps are drawn in the same way as in figure 1.

this refinement. This result corresponds to the electronic state $(t_{2g})^{4\cdot75}(e_g)^{2\cdot25}$ and the low-spin model is unequivocally excluded. In fact, the difference map after the refinement with low-spin model (figure 3) gave very high positive peaks near the Co nucleus.

3.1.2. *$KFeF_3$ (Miyata* et al. *1983)*

The deformation densities around the Fe^{2+} ion in an octahedral field were analysed in terms of aspherical scattering factors. The refinement assuming the high-spin state for the Fe^{2+} ion decreased the R value to 0·0072 from 0·0075 obtained with the spherical scattering factors, while that assuming low-spin state $(t_{2g})^6(e_g)^0$ increased the value to 0·0142. Further refinement of electron populations for t_{2g} and e_g orbitals gave the electronic state as $(t_{2g})^{3\cdot93}(e_g)^{2\cdot07}$. Thus the high-spin model is a good approximation to the electronic state of Fe^{2+}.

3.1.3. *$KNiF_3$ and $KMnF_3$ (Kijima* et al. *1983)*

The refinement with aspherical scattering factors for 3d orbitals revealed that the Ni^{2+} ion is in the $(t_{2g})^6(e_g)^2$ state and Mn^{2+} ion is in the high-spin state $(t_{2g})^3(e_g)^2$, both to good approximations. The refinement assuming the high-spin state for the Mn^{2+} ion gave the final R value of 0·012, while that assuming the low-spin state increased the R value to 0·0213. A close inspection of the residual density around the Mn^{2+} ion revealed the evidence of anharmonic vibration of Mn^{2+}. The analysis of the anharmonic thermal vibration in this crystal was successfully carried out (unpublished result).

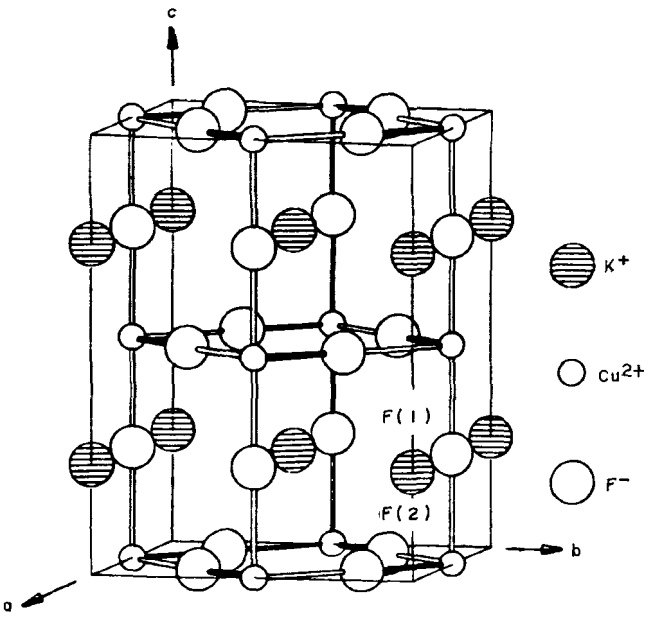

Figure 4. Crystal structure of $KCuF_3$ (type a). Bold lines indicate short Cu–F_s bonds. The unit cell is drawn by fine single lines.

3.1.4. *$KCuF_3$ (Tanaka* et al. *1979, Tanaka and Marumo 1982)*

Crystals of $KCuF_3$ are dimorphous and have perovskite structures: type a and type b (Okazaki 1969a, b). Figure 4 illustrates more common type a structure (Okazaki and Suemune 1961). In this structure the F(2) atom is displaced from the midpoint between two neighbouring Cu atoms in the *a–b* plane, forming a short and a long Cu–F bond. The Cu–F(1) distance lies between the two Cu–F(2) distances but is much closer to the shorter one. Accordingly, the coordination octahedron of the Cu atom has pseudo-tetragonal symmetry. In the following discussion the F atoms at the longest, intermediate and shortest distances are denoted as F_l, F_m and F_s respectively. Such distortion is attributed to a cooperative Jahn–Teller effect (Kanamori 1960) and the

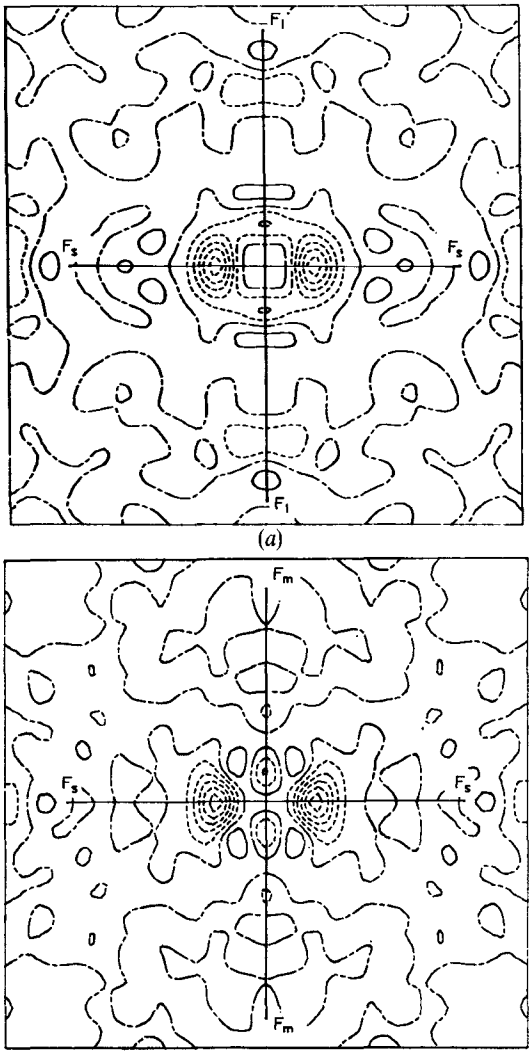

Figure 5. The sections of the deformation density of $KCuF_3$ after the refinement with the spherical scattering factors. (*a*) The section through the Cu–F_s and Cu–F_l bonds. (*b*) Section through the Cu–F_s and Cu–F_m bonds. Contours are drawn in the same way as in figure 1.

direction of the displacements of F(2) atoms alternate along the c axis, doubling the c period of the cubic perovskite structure. Preliminary refinement of the structure (Tanaka *et al.* 1979) revealed large negative troughs around the Cu atom on the deformation density map, which seemed to indicate the distribution of the hole on the Cu^{2+} ion in an octahedral field by the Jahn–Teller effect. In an ideal tetragonal field, the fivefold-degenerate orbitals split into four levels: a doubly degenerate orbital composed of d_{xz} and d_{yz}, and three non-degenerate orbitals, d_{xy}, d_{z^2} and $d_{x^2-y^2}$ orbital in the ground state of a Cu^{2+} ion. The quantization axis was taken along the Cu–F_1 bond. Figure 5 shows the deformation density around the Cu^{2+} ion. A large trough of $-1{\cdot}57\,e\,Å^{-3}$ is observed on the Cu–F_s bond at 0·52 Å from the Cu^{2+} nucleus, while a positive peak of $0{\cdot}37\,e\,Å^{-3}$ exists on the Cu–F_1 bond at 0·62 Å from the central Cu^{2+} nucleus. On the Cu–F_m bond only a small negative trough is observed near Cu^{2+}

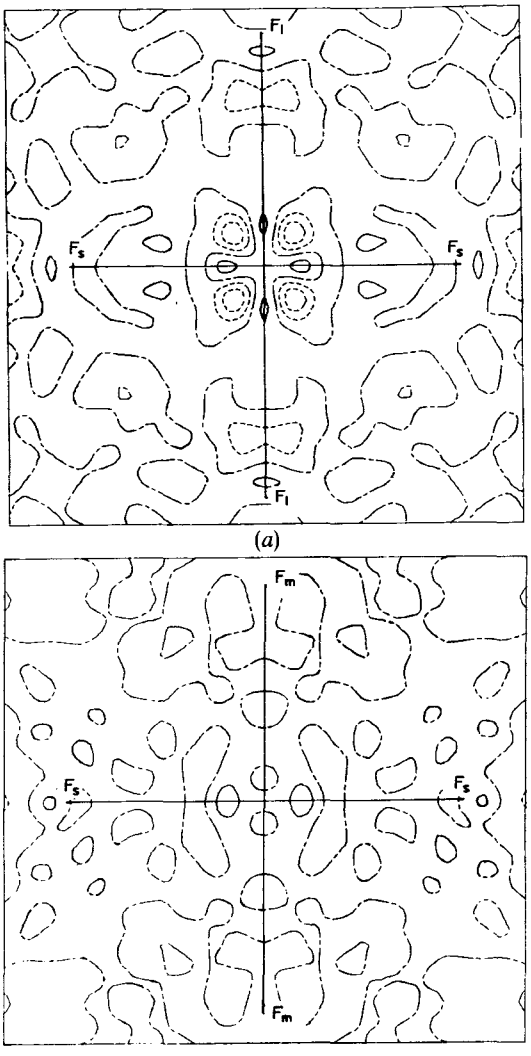

Figure 6. The sections of the difference maps after the refinement assuming a cooperative Jahn–Teller effect. The contours are drawn in the same way as in figure 1.

nucleus. These features roughly agree with the electron configuration model described above. However, this model is not satisfactory because a small but significant difference exists between the Cu–F_m and Cu–F_s bonds. Namely, Cu^{2+} is located in a crystal field with orthorhombic symmetry. The distortion is ascribed to a cooperative Jahn–Teller effect, and it is necessary to consider the linear combination of d_{z^2} and $d_{x^2-y^2}$ orbitals to express the electronic state.

$$\psi_g = \cos(\varphi/2)\, d_{z^2} + \sin(\varphi/2)\, d_{x^2-y^2},$$

$$\psi_e = \sin(\varphi/2)\, d_{z^2} - \cos(\varphi/2)\, d_{x^2y^2}.$$

Refinement assuming such an orthorhombic Jahn–Teller distortion reduced the R factors significantly. The value of $\cos(\varphi/2)$ was 0·908(17), where the thermal motion of the 3d electrons was refined separately from that of the core electrons. This value agrees with the theoretically estimated value (Kadota *et al.* 1967). Figure 6 shows the

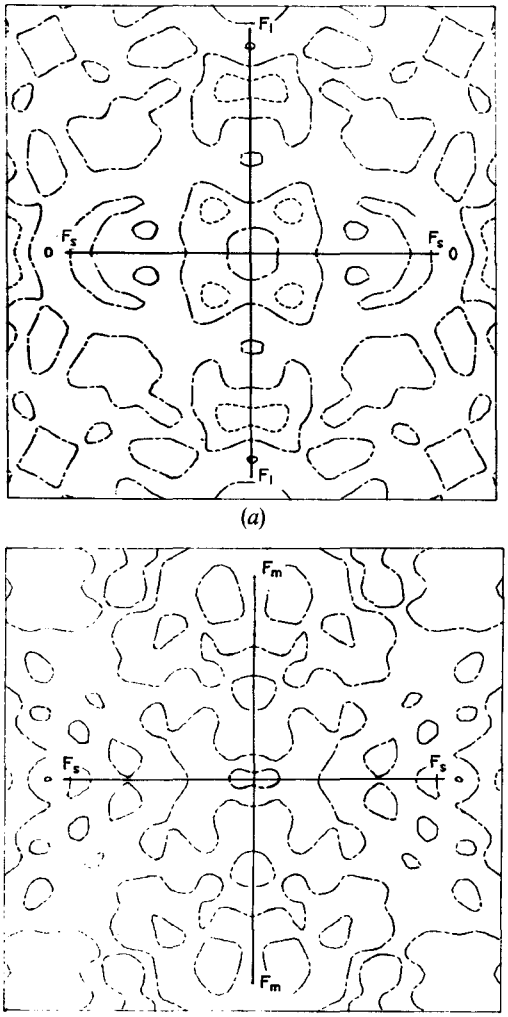

Figure 7. The sections of the difference maps after the refinement, taking the anharmonic vibration of the Cu atom into account. The contours are drawn in the same way as in figure 1.

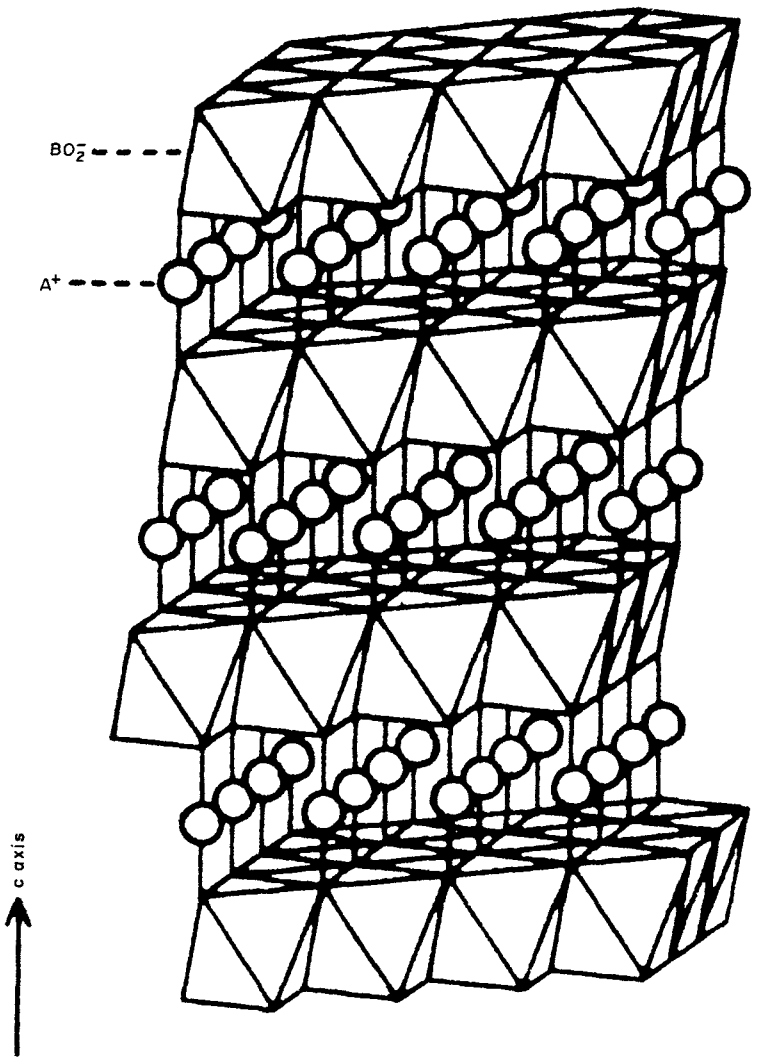

Figure 8. Schematic view of the delaffossite structure ABO_2, showing the linkage of the BO_6 octahedra.

difference density map at this stage. Two large troughs on Cu–F_s bond were deleted, and the positive and negative peaks around the Cu^{2+} ion were reduced in peak heights, however, new positive peaks appeared on Cu–F_s bonds. These were ascribed to anharmonic vibration of the Cu^{2+} ion. Anharmonic vibration of the Cu^{2+} ion with the point group symmetry mmm was analysed using Willis's method (1969) (Tanaka and Marumo 1982). The obtained one-particle potential has small but significant anharmonicity. The analysis diminished newly emerged peaks on difference maps, indicating that their origin was the anharmonic vibration of the Cu^{2+} ion (figure 7). Thus peaks on difference maps could be separated into those due to asphericity of d electron density placed in a crystal field and those due to anharmonic thermal vibration.

3.1.5. *$CuAlO_2$ (Ishiguro* et al. *1983)*

Crystals of $CuAlO_2$ have a delaffosite ($CuFeO_2$) structure, containing the Cu^+ ion with linear twofold coordination. It has a general formula $A^+B^{3+}O_2^{2-}$ and the structure is very anisotropic. Figure 8 depicts a schematic view. It is constructed by the alternate stacking of edge-shared $\{BO_2^-\}_\infty$ octahedral layers and A^+ ion layers perpendicular to the c axis. Each A^+ ion is coordinated linearly by two O^{2-} ions. The A^+ ion is restricted to a d^{10} or a d^9 ion, while a number of trivalent cations can be accommodated in the octahedral site. The spatial distribution of 3d electrons has been investigated for $CuAlO_2$. Figures 9(*a*) and (*b*) show the deformation density after refinement with spherical scattering factors. A large negative trough with a depth of $-0{\cdot}7\,e\,Å^{-3}$ is observed on the Cu–O bond at 0·45 Å from the Cu^+ ion (figure 9(*b*)), whereas on the plane $z=0$ (figure 9(*a*)) a circular positive region with a maximum height of $0{\cdot}3\,e\,Å^{-3}$ (at 0·23 Å from the Cu^+ ion) surrounds the Cu nucleus, and a negative region with a maximum depth of $-0{\cdot}4\,e\,Å^{-3}$ (at 0·49 Å from Cu^+ on the Cu–Cu bonds) is observed outside the positive region. Further positive peaks with heights of $0{\cdot}4\,e\,Å^{-3}$ lie at 0·71 Å from Cu^+ on the lines bisecting the angles between two neighbouring Cu–Cu bonds. These features roughly agree with Orgel's electron-configuration model of the d–s hybridization (Orgel 1966).

As suggested by Orgel (1966) and Rogers *et al.* (1971), d–s hybridized orbitals for the linear twofold coordination of a Cu^+ ion can be represented as follows:

$$\psi_{d-ks}=\frac{1}{(1+k^2)^{1/2}}(d_{z^2}-ks) \quad \text{for a fully occupied orbital,}$$

$$\psi_{d+ks}=\frac{1}{(1+k^2)^{1/2}}(d_{z^2}+ks) \quad \text{for a non-occupied one,}$$

where k is a parameter to measure the degree of contribution of the 4s orbital. This refinement significantly reduced the R value from 0·011 to 0·0101, giving a value of 0·25(2) for k.

Figure 10 shows the difference maps after this refinement. The troughs on the Cu–O bonds and the circular positive region on the plane $z=0$ disappeared on the maps. However, the positive and negative isolated peaks on the plane $z=0$ did not vanish though they were reduced in magnitudes, and new positive peaks appeared on the Cu–O bonds with height $0{\cdot}3\,e\,Å^{-3}$ at 0·30 Å from the Cu^+ ion. All of these peaks disappeared completely after the refinement assuming anharmonic vibration of the Cu^+ ion.

3.1.6. *[Cu(diazacyclooctane)$_2$](NO$_3$)$_2$ (Tanaka and Marumo 1990)*

The aspherical density obtained by multipole refinement does not represent the wavefunctions, because they do not fulfill orthonormal conditions. Recently a conventional least-squares method was improved to obtain the representation of wavefunctions (Tanaka 1988). It can be applied to both the atomic-orbital and the molecular-orbital methods. The method was applied to the wavefunction analysis of the Cu^{2+} ion in $[Cu(diazacyclooctane)_2](NO_3)_2$. The wavefunction in a crystal field *Ci* was obtained by optimizing the charge density distribution. Table 1 lists the obtained κ parameters and the orbital coefficients for the five d orbitals. κ is a factor multiplying the radial coordinates, allowing expansion or contraction of the valence shell. As shown in table 1, the orbitals lying in the coordination plane contract ($\kappa>1$), while those perpendicular to it expand ($\kappa<1$).

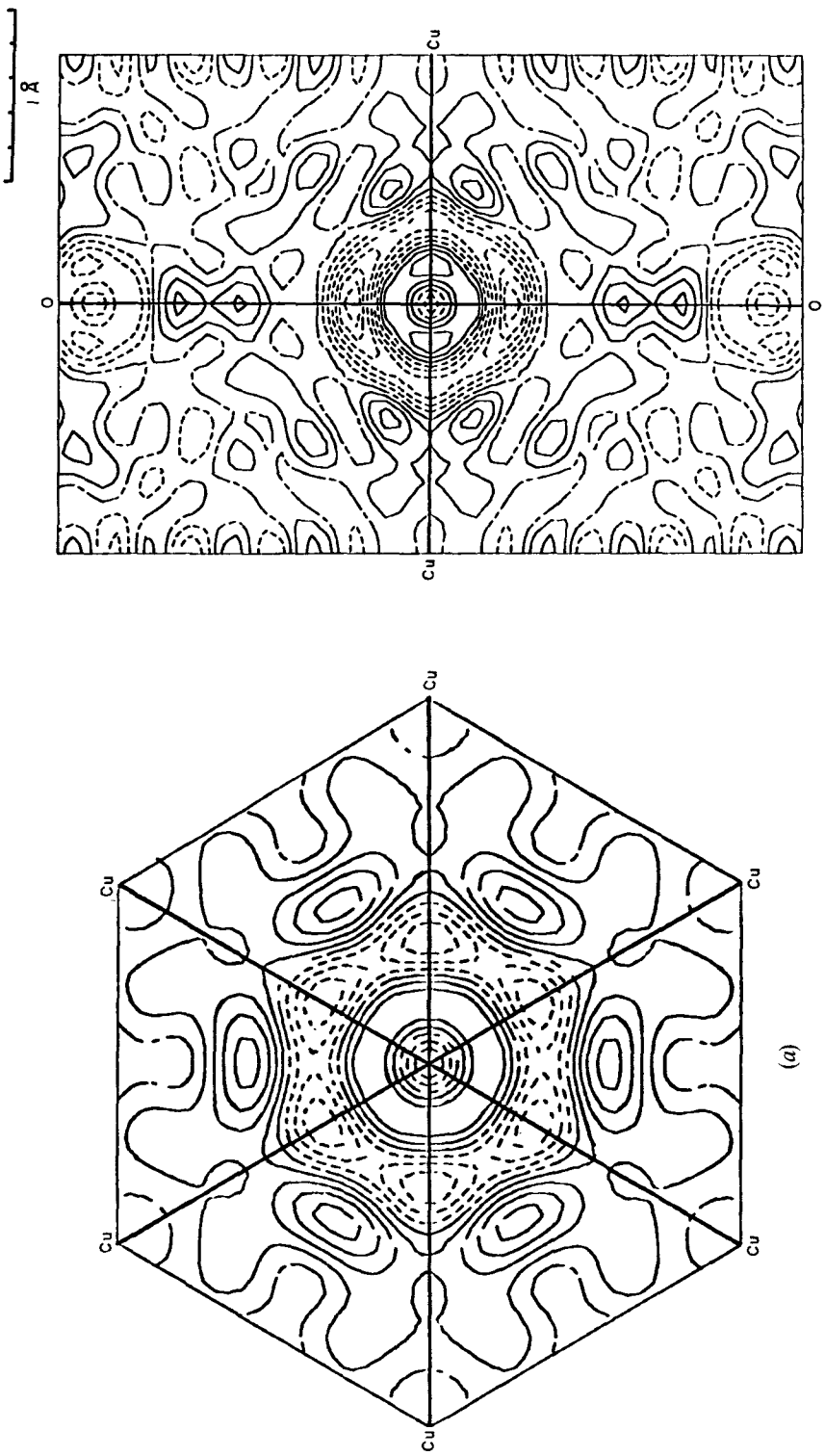

Figure 9. The sections of the deformation density of $CuAlO_2$ after refinement with spherical scattering factors. The contours are drawn at intervals of 0·1 e Å^{-3}. Negative (- - -) and zero (— · —) contours. (*a*) Section $z = 0$, (*b*) Section $y = 0$. Cu atom lies at the centre. Cu or O indicates the directions of the adjacent atom.

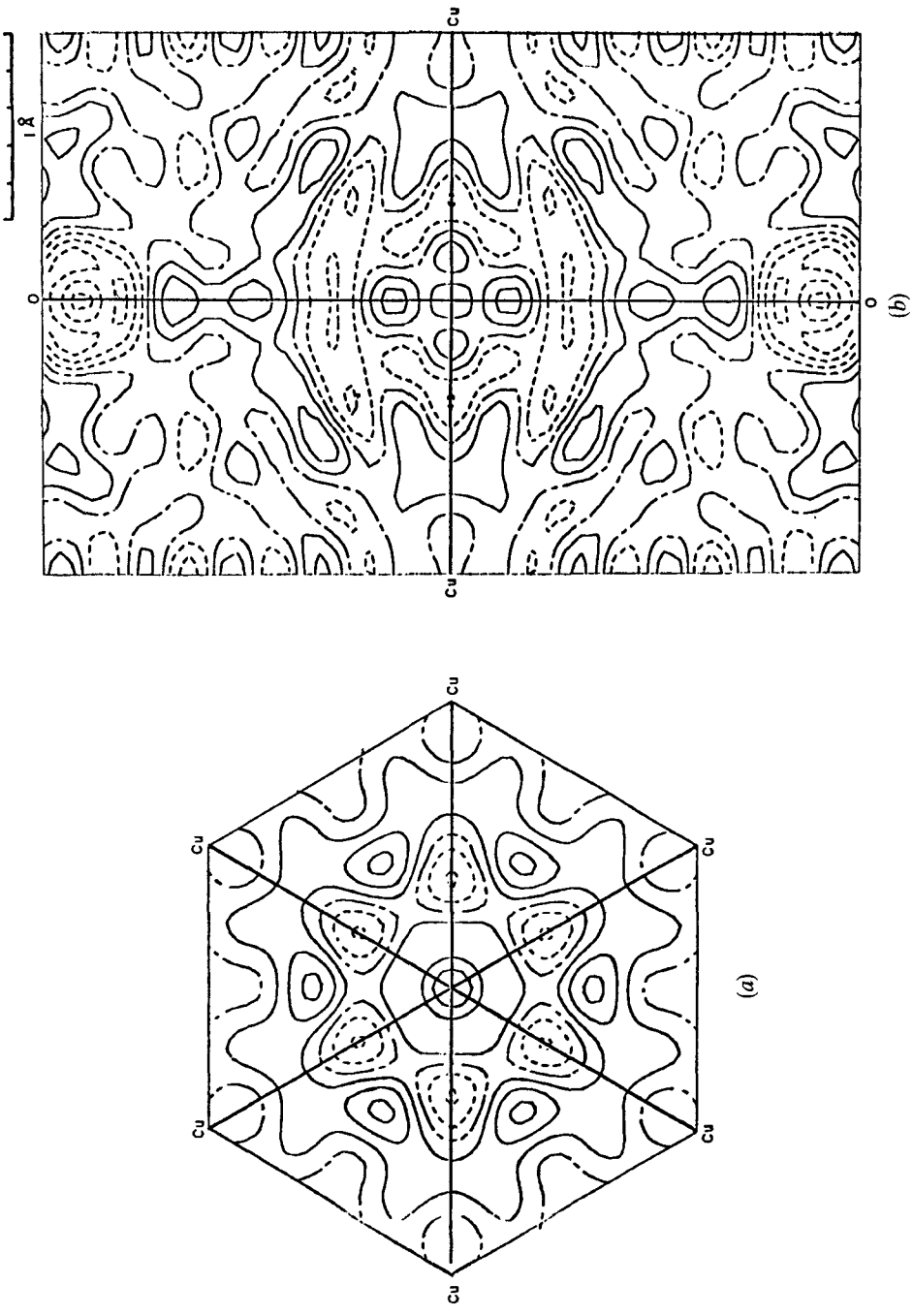

Figure 10. The sections of the difference map after the refinement assuming d–s hybridization of the Cu atom. The contours are drawn at intervals of 0·1 e Å^{-3}.

Table 1. Orbital coefficients for the five orbitals of the Cu atom in $[Cu(diazacyclooctane)_2]^{2+}$.

No.	Electron population	κ	$d_{x^2-y^2}$	d_{z^2}	d_{yz}	d_{zx}	d_{xy}
1	1·0	0·97(11)	0·81(46)	0·20(76)	0·17(178)	0·52(105)	−0·06(79)
2	2·0	1·37(7)	−0·07(28)	0·11(17)	−0·24(20)	0·03(25)	−0·96(6)
3	2·0	0·81(5)	0·48(33)	0·12(48)	−0·62(45)	−0·59(46)	0·11(21)
4	2·0	0·71(4)	0·15(26)	−0·92(11)	−0·28(36)	0·21(38)	−0·04(11)
5	2·0	0·90(5)	0·29(78)	−0·28(45)	0·67(52)	−0·58(76)	−0·23(20)

3.2. *4d electron density*

In spite of a very small valence/metal electron ratio, the asphericity of even 4d and 5d electrons in a ligand field has been successfully detected by a careful study.

Electron-density distributions in crystals of $K_2[PdCl_4]$ and $K_2[PdCl_6]$ were obtained based on the intensities collected at 120 K (Takazawa *et al.* 1988). Figures 11 (*a*) and (*b*) show the sections of the deformation densities of square-planar $[PdCl_4]^{2-}$ ion on the (100) plane and the (001) plane (coordination plane) through the Pd atom. In figure 11 (*a*), positive peaks of $+2{\cdot}3(3)\,e\,Å^{-3}$ are located on the fourfold axis at 0·47 Å from the Pd nucleus, whereas negative troughs of $-1{\cdot}0(2)\,e\,Å^{-3}$ are located on the Pd–Cl bond axis at 0·36 Å from the Pd nucleus. They indicate excess 4d electron popuation for the $a_{1g}(d_{z^2})$ orbital and the lack of $b_{1g}(d_{x^2-y^2})$ orbital population. In figure 11 (*b*) there exist positive peaks of $0{\cdot}8(2)\,e\,Å^{-3}$ on the direction bisecting the Cl–Pd–Cl angle, which show excess 4d electron population for the $b_{2g}(d_{xy})$ orbital. Figures 12 (*a*) and (*b*) illustrate the deformation densities of the octahedral $[PdCl_6]^{2-}$ ion. In figure 12 (*a*) there are positive peaks of $1{\cdot}4(3)\,e\,Å^{-3}$ on the threefold axes at 0·51 Å from the Pd nucleus, and negative troughs of $-1{\cdot}0(2)\,e\,Å^{-3}$ on the Pd–Cl bond axes at 0·48 Å from the Pd nucleus. They indicate excess 4d electron population for the t_{2g} orbitals and deficiency in the e_g orbitals. Figure 12 (*b*) shows the section at the face of the cube, on the apices of which the positive deformation density has its maximum (Saito 1979). This feature is almost the same as that observed for the octahedral complex $[Co(NO_3)_6]^{3-}$ (Ohba *et al.* 1978). Deformation densities at room temperature (300 K) show similar features. The peak positions are almost the same at 300 K and 120 K. The peak heights at 300 K are less than half of those at 120 K because of the larger thermal motion. This implies that the charge asphericity is due, not to the thermal vibration of the central metal atom, but to the 4d electrons. The observed charge asphericities could be reproduced by the multipole expansion method with reasonable d orbital populations (Hansen and Coppens 1978). Table 2 lists the electron populations in each of the orbitals of Pd. Effective charges of the Pd atom were also estimated by direct integration; the values are shown in table 3. The effective radius of Pd was estimated to be 1·2 Å for both complexes from the minimum of the radial distribution (see figure 13). The observed radial distributions have a shoulder at about 0·5 Å, which corresponds to the 4d electrons. The effective charges derived by electron spectroscopy for chemical analysis (ESCA) and nuclear quadrupole resonance (NQR) are also listed in table 2 for comparison. The effective charges indicate that the central metal atoms are largely neutralized by donation of electrons from the ligating atoms.

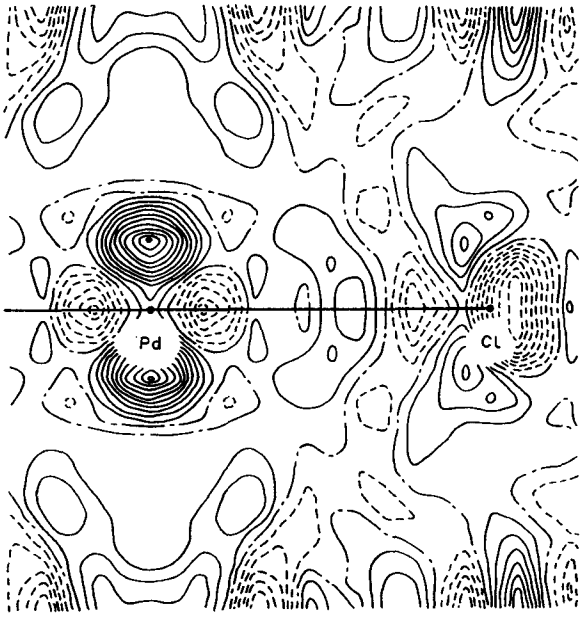

(*a*)

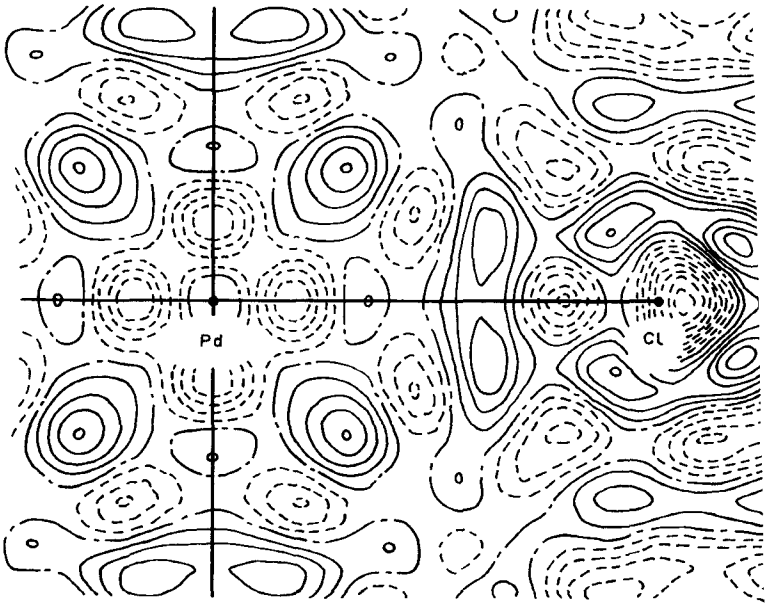

(*b*)

Figure 11. Deformation densities of $[PdCl_4]^{2-}$ at 120 K. (*a*) On the (100) plane and (*b*) on the (001) plane. Contour intervals at 0·2 e Å^{-3}. Negative contours broken, zero contours chain-dotted.

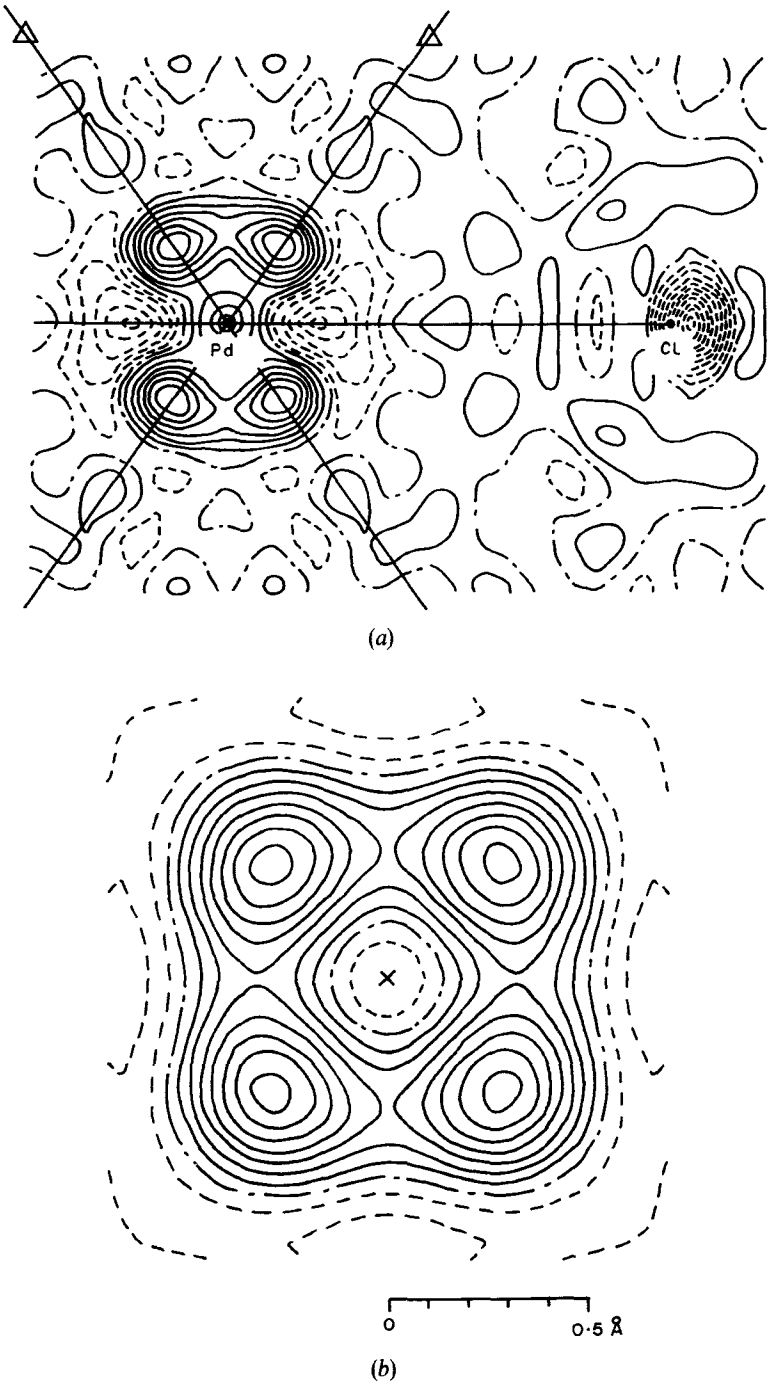

Figure 12. Deformation densities of $[PdCl_6]^{2-}$ at 120 K. (*a*) On the (110) plane and (*b*) through the plane perpendicular to the Pd–Cl bond axis at 0·30 Å from the Pd nucleus. The cross indicates the location of the Pd–Cl bond. Contours are drawn in the same way as in figure 11.

Table 2. Electron population in each of orbitals of Pd. Refinement A: populations are not constrained; B: populations of a_{1g} and e_g orbitals are fixed; C: populations of a_{1g}, e_g and b_{2g} orbitals are fixed.

$[PaCl_4]^{2-}$	A	B	C
$b_{1g}(d_{x^2-y^2})$	1·13(5)	1·69(3)	1·49(1)
$b_{2g}(d_{xy})$	1·93(5)	2·25(3)	2·0
$e_g(d_{xz}, d_{yz})$	4·49(6)	4·0	4·0
$a_{1g}(d_{z^2})$	2·41(5)	2·0	2·0
Total	9·96(6)	9·94(6)	9·49(3)
$[PdCl_6]^{2-}$			
$e_g(d_{x^2-y^2}, d_{z^2})$	1·89(7)		
$t_{2g}(d_{xy}, d_{xz}, d_{yz})$	6·14(8)		
Total	8·03(10)		

Table 3. Effective charge of Pd.

	Formal	MR†	DI‡	ESCA	NQR
$[PdCl_4]^{2-}$	+2	+0·51(3)	+0·55(35)	+0·4(2)§	
$[PdCl_6]^{2-}$	+4	+1·97(10)	+1·16(41)	+1·4(1)‖	+0·58¶

† Multipole refinement.
‡ Direct integration.
§ Forkesson and Larsson (1976).
‖ Larsson and Forkesson (1977).
¶ Ito *et al.* (1961).

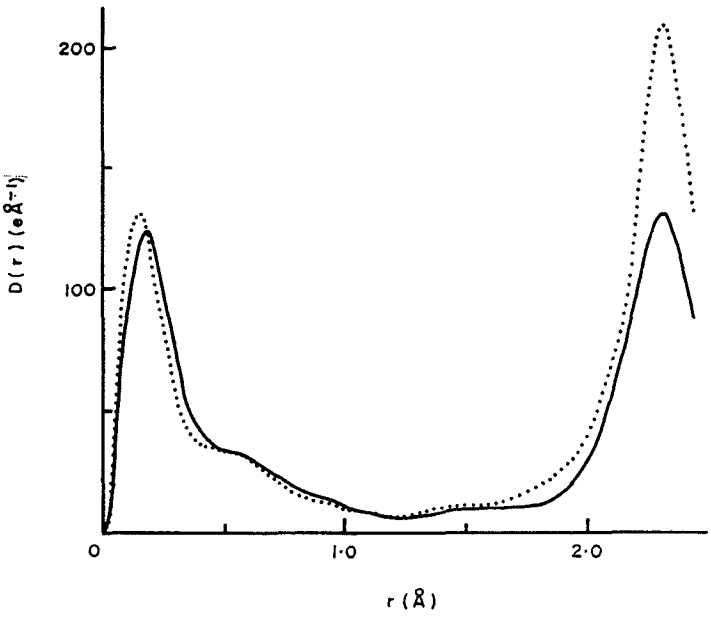

Figure 13. Radial distribution curves for $[PdCl_4]^{2-}$ (solid line) and $[PdCl_6]^{2-}$ (dotted lines).

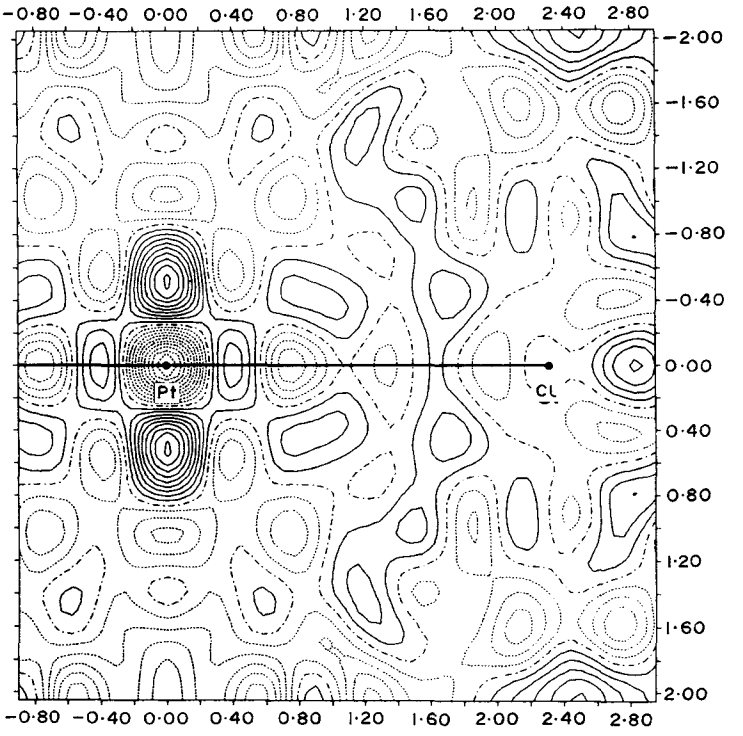

(*a*)

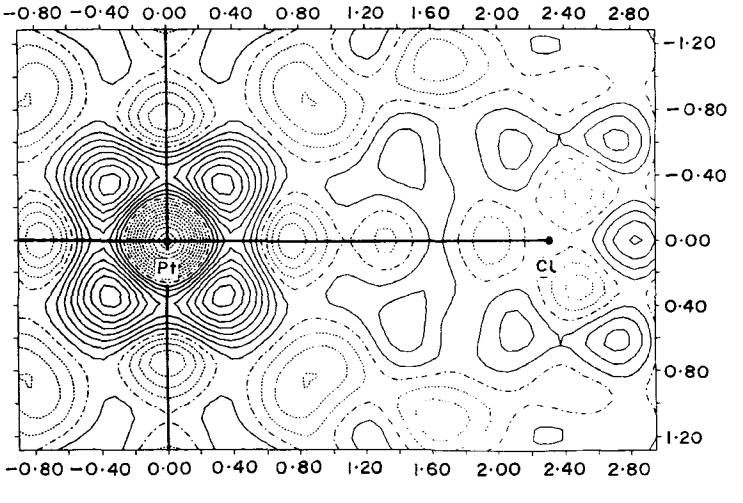

(*b*)

Figure 14. Deformation densities of $[PtCl_4]^{2-}$ at 120 K. (*a*) On the (100) plane and (*b*) on the (001) plane. Contours are drawn in the same way as in figure 11.

3.3. *5d electron density* (*Takazawa* et al. *1990*)

As for 5d transition metal complexes, square-planar and octahedral chloro-complexes were examined: K_2PtCl_4 and K_2PtCl_6. Ag Kα radiation ($\lambda = 0{\cdot}56083$ Å) monochromatized by LiF was also used to collect the intensity data in order to avoid high absorption of Mo Kα radiation by the Pt atom. All the data collections were carried out at 120 K. Figures 14 (*a*) and (*b*) give the sections of the deformation densities of $[PtCl_4]^{2-}$ ion on the (100) plane and (001) plane, the latter being the coordination plane. The general features of the asphericity are largely similar to figures 11 (*a*) and (*b*). The two peaks ($1{\cdot}8\,e\,Å^{-3}$, 0·52 Å from the Pt nucleus) above and below the coordination plane indicate excess electron density in the $a_{1g}(d_{z^2})$ orbital, whereas four troughs ($-0{\cdot}8\,e\,Å^{-3}$, 0·75 Å from Pt) on the Pt–Cl bonds show the deficiency of electron density in $b_{1g}(d_{x^2-y^2})$ orbitals. Figure 15 gives the residual electron density for $[PtCl_6]^{2-}$. The arrangement of four peaks ($+1{\cdot}1(3)\,e\,Å^{-3}$, 0·62 Å from Pt) resembles that observed for $[PdCl_6]^{2-}$, indicating excess electron density in the t_{2g} orbitals and the deficiency of electron density in the e_g orbitals. These features are quite similar to those observed for 3d and 4d complexes. Effect of anharmonic thermal vibrations of the Pt atom do not affect the deformation maps. Table 4 lists the effective charges of the Pt estimated by electron population analysis and by direct integration of the electron density. The effective radius of Pt was taken to be 1·2 Å. The effective charges derived by other methods are also included in table 4. The results indicate that the central Pt atom is largely neutralized by electron donation from the ligating atoms, though the definition of the effective charge differs according to the method of measurements.

Population analyses of 4d and 5d electrons in Pd and Pt complexes indicated contraction of the valence orbitals on complex formation ($\kappa > 1$), which agreed with the theoretical calculation by the discrete variational (DV) Xα MO self-consistent-charge method. This may be the reason why rather diffuse 4d and 5d electron distribution can be detected.

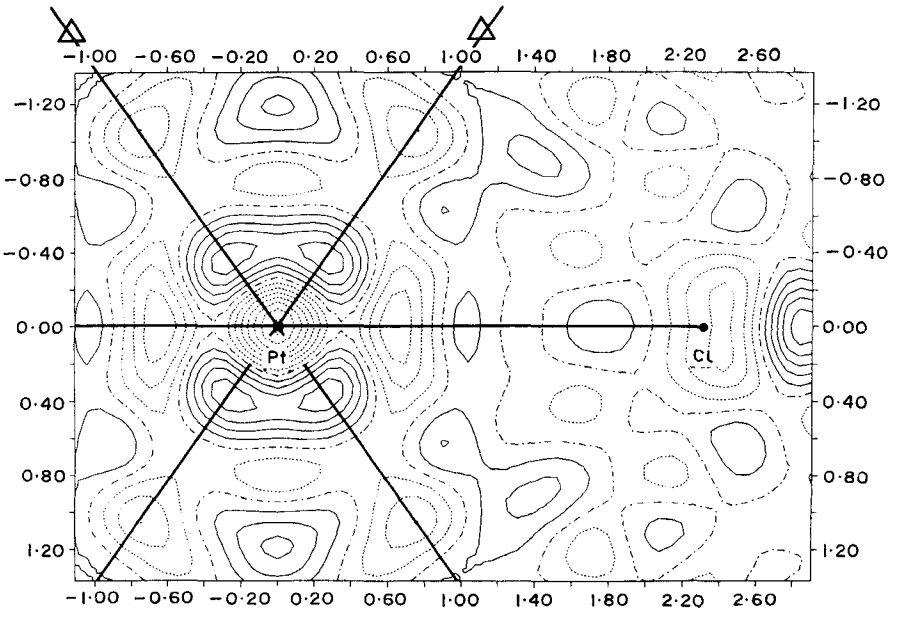

Figure 15. Deformation density of $[PtCl_6]^{2-}$ at 120 K on the (110) plane. Contours are drawn in the same way as in figure 11.

Table 4. Effective charge of Pt.

	Formal	MR	DI	ESCA	NQR
$[PtCl_4]^{2-}$	+2	+1·67(6)†	+1·0(3)†	+0·4(2)‡	+0·4§
$[PtCl_6]^{2-}$	+4	+1·03(15)†	+1·3(8)†	+1·3(1)‖	+0·64¶
					+0·70*

† Ag Kα data.
‡ Forkesson and Larsson (1976).
§ Marram *et al.* (1963).
‖ Larsson and Forkesson (1977).
¶ Nakamura *et al.* (1960).
* Brown *et al.* (1970).

4. Magneto-structural interaction in dimeric copper carboxylate adducts

Dimeric copper(II) carboxylate adducts of the general formula $[Cu(RCOO)_2L]_2$ have the structure shown in figure 16. The temperature-dependent magnetic susceptibility and electron paramagnetic resonance (EPR) of the acetate complex ($R=CH_3$, $L=H_2O$) could be explained by a model involving isolated pairs of copper ions interacting strongly through exchange forces, each pair forming a lower singlet state and an excited triplet state (Bleaney and Bowers 1952). A measure of the magnetic interaction is the singlet–triplet separation, $-2J$. X-ray structural analysis (van Niekerk and Schoening 1953) which employed two-dimensional photographic data revealed a Cu–Cu distance of 2·64 Å, which is shorter than the Cu–Cu distance of 2·556 Å in metallic copper. This short Cu–Cu bond was astonishing at that time. Several workers at times thought that this complex possessed a weak metal–metal

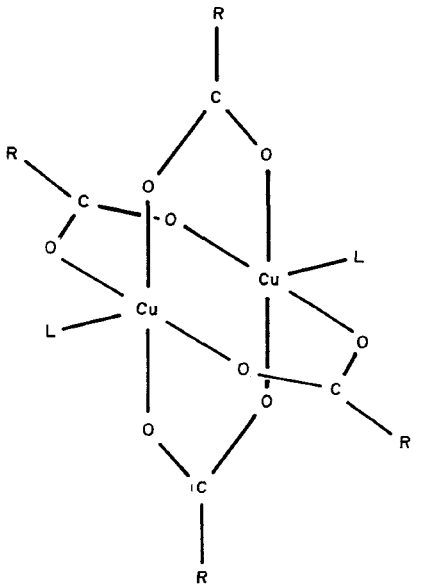

Figure 16. Dimeric copper(II) carboxylate adduct, $[Cu(RCOO)_2L]_2$.

bond and it was this bond that led to the antiferromagnetic interaction characterized by $-2J$ of 284 cm^{-1} (Guha 1951). At present, however, it is generally believed that a superexchange interaction is present. The 'tails' of the acetate orbitals provide the exchange pathway between the two metal magnetic orbitals and there is very little, if if any, of a direct metal–metal exchange pathway in this complex. The discussion about the exchange pathway in this complex stimulated many physical chemists and a number of papers were published on the preparation and characterization of a large number of dimeric copper(II) carboxylate adducts (Kato *et al.* 1964, Doedens 1976, Moreland and Doedens 1978, Melnik 1982, Kato and Muto 1988). There have been two re-investigations (Brown and Chidambaram 1973, Kishita *et al.* 1964) of the crystal structure of the copper(II) acetate dimer ($R = CH_3$, $L = H_2O$) and these studies revealed a Cu–Cu distance of 2·626 (1) Å. All the dimeric copper(II) carboxylate complexes show moderately strong antiferromagnetic interactions and their $-2J$ values range from 216 cm^{-1} ($R = CCl_3$, L = 2-chloropyridine) (Moreland and Doedens 1978) to about 500 cm^{-1} (R = H, L = urea) (Kishita *et al.* 1964, Yawney and Doedens 1970). A number of attempts have been made to correlate the magnetic behaviour with structural (Cu–Cu and O–C–O distances, Cu–Cu–L and O–Cu–L angles) and physical properties such as pK_a of parent carboxylic acids, R group polarizabilities, but success has been limited. The antiferromagnetic interaction in $[Cu(RCOO)_2L]_2$ is known to have a trend to increase as either the axial ligand, L, or the carboxylate substituent, R, becomes a stronger electron donor (Jotham *et al.* 1972). In fact, dimeric copper(II) formates, having a stronger parent acid ($pK_a = 3{\cdot}75$), show much larger $-2J$ values (about 500 cm^{-1}) than the corresponding copper(II) acetate dimers, having a weaker parent acid ($pK_a = 4{\cdot}75$), whose $-2J$ value is about 300 cm^{-1} (Hay *et al.* 1975).

To compare the structures of dimeric copper formates and acetates as precisely as possible, the following eight $[Cu(RCOO)_2L]_2$ complexes were selected and the crystal structures were carefully investigated:

I.	$R = CH_3$, L = pyridine* orthorhombic modification	**V.**	$R = CH_3$, L = β-picolone
II.	$R = CH_3$, L = pyridine* monoclinic modification	**VI.**	R = H, L = β-picolone
III.	$R = CH_3$, L = urea*	**VII.**	$R = CH_3$, L = γ-picoline
IV.	R = H, L = urea*	**VIII.**	R = H, L = γ-picoline

Those marked with an asterisk are re-investigations by Uekusa *et al.* (1989), the remainder have been investigated by Yamanaka *et al.* (1990).

Figure 17 illustrates some of the molecular structures. The original large R values ranging from 0·167 to 0·089 are probably due to limited precision of the photographic data. The present study achieved much lower R values, from 0·022 to 0·051, and reduced the e.s.d.s in the atomic parameters to a quarter by collecting and averaging symmetry-related reflections and preparing spherical crystals where possible. In table 5 the average dimensions of the $Cu_2(RCOO)_4$ cage in $[Cu(RCOO)_2L]_2$ and $-2J$ values are tabulated, where the data for (R = H, L = pyridine) are also included (Bernard *et al.* 1979). The values of $-2J$ were determined by one of the authors (M.K.) by the Faraday method in the temperature range 80–300 K. The cryomagnetic data fittings to the Bleaney–Bowers equation were made with the SALS program using a fixed value of

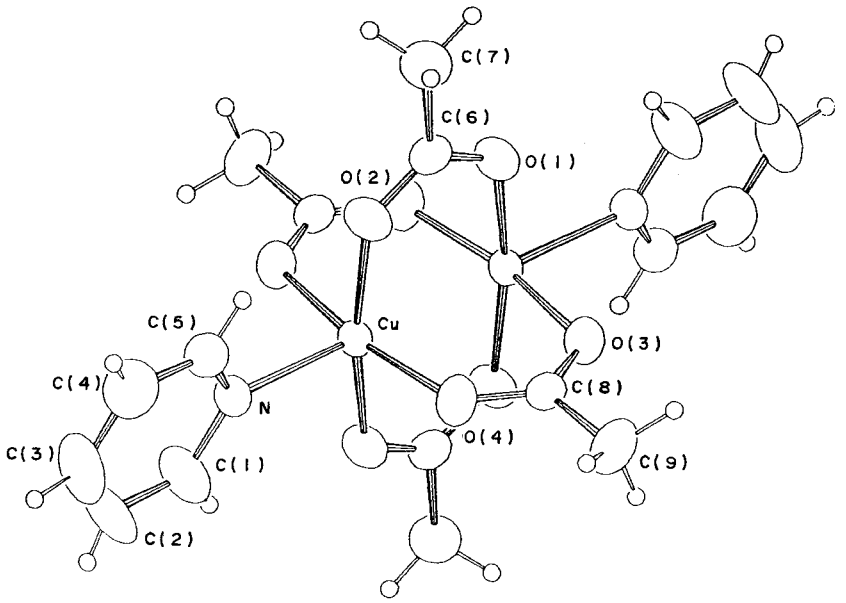

I.

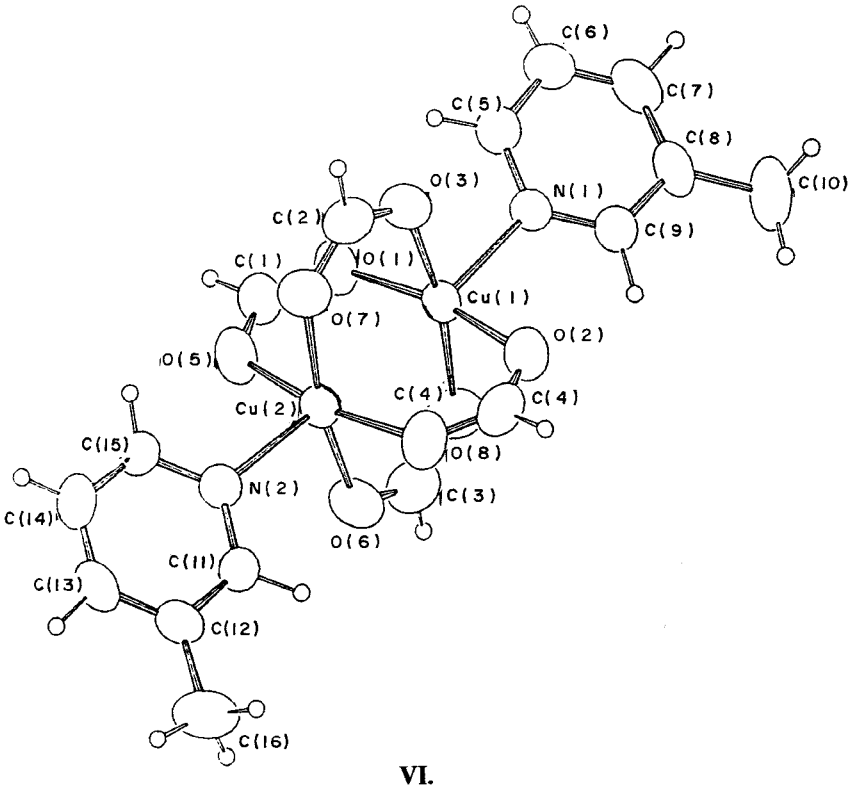

VI.

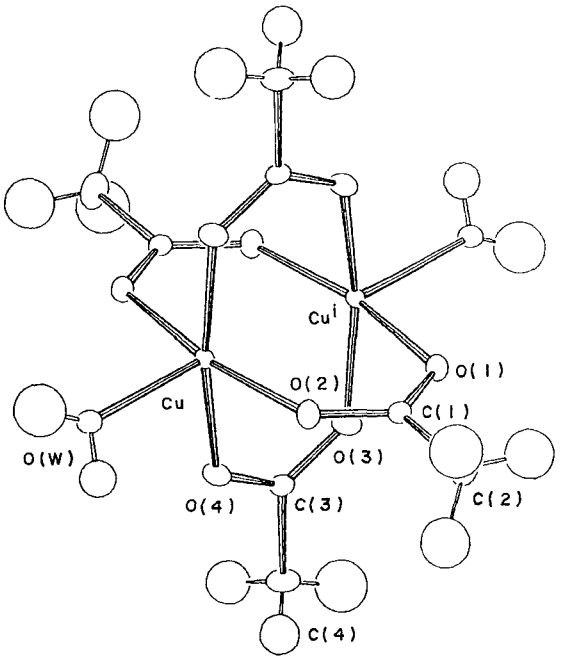

IX.

Figure 17. ORTEP drawings (Johnson 1965) of the molecules with thermal ellipsoids scaled at the 50% probability level. H atoms are represented by circles of radius 0·08 Å for **I** and **VI**. **I** and **VI**: room temperature, **IX**: 120 K.

60×10^{-6} e.m.u. for temperature independent paramagnetism, N_{α}. As a convenient statistical measure of the quality of the least-squares fits, the discrepancy index,

$$\sigma_{dis} = \left[\frac{\Sigma(\chi_{obsd} - \chi_{calc})^2}{\Sigma \chi^2_{obsd}}\right]^{1/2},$$

was employed. The values of σ_{dis} ranged from 2×10^{-3} to 4×10^{-3}, showing the high quality of the fits. The $-2J$ value for **III** was obtained for the anhydrous form. The values of $-2J$ for Cu(II) acetate-pyridine were determined on a mixture of **I** and **II**. However, the discrepancy index, $2{\cdot}2 \times 10^{-3}$, indicates that the $-2J$ values of these two forms are almost identical.

These structural studies confirmed that there exist no structural correlations with the magnitudes of the superexchange interactions. In formates, the mean Cu–O distance in the cage is longer by 0·003 Å, and the Cu–L length (the distance between Cu and the coordinating atom of the ligand) shorter by 0·021 Å than those in acetates. These small differences do not seem to affect the magnetic properties, since there is the same order of variation between the orthorhombic (I) and monoclinic (II) structures of $[Cu(CH_3COO)_2py]_2$, the difference in Cu–O and Cu–L bond lengths being 0·002(3) and 0·028(4) Å respectively. The greater $-2J$ value for copper (II) formate was tentatively attributed to its shorter Cu–O bond length, based on the structural data of $[Me_4N]_2[Cu(RCOO)_2(NCS)]_2$ (R = H and CH_3) (Goodgame *et al.* 1969).

Table 5. A comparison of the average dimensions of the $Cu_2(RCOO)_4$ cage in $[Cu(RCOO)_2L]_2$. Bond lengths in Ångström units, bond angles in degrees and $-2J$ in reciprocal centimetres.

				$R=CH_3$	R=H
	$R=CH_3$, L=py		R=H	L=ur	L=ur
	(I) orthorhombic	(II) monoclinic	L=py†	(III)	(IV)
Cu···Cu	2·641(1)	2·628	2·663(1)	2·624(1)	2·655(1)
Cu–L	2·191(2)	2·163(4)	2·145(2)	2·135(1)	2·120(2)
Cu–O	1·972(3)	1·974(3)	1·981(2)	1·970(2)	1·977(2)
C–O	1·253(4)	1·252(4)	1·245(3)	1·253(2)	1·245(3)
Shift of Cu‡	0·208(1)	0·207(3)	0·207(1)	0·200(1)	0·213(1)
Cu–O–C	123·4(2)	123·4(3)	122·5(2)	123·7(1)	122·6(2)
O–C–O	125·2(3)	124·8(4)	127·0(3)	124·5(2)	127·2(2)
$-2J$§	333·0		501·0	323·0	506·0

	$R=CH_3$	R=H	$R=CH_3$	R=H
	(V) L=β-pic	(VI) L=β-pic	(VII) L=γ-pic	(VIII) L=γ-pic
Cu···Cu	2·628(2)	2·694(1)	2·641(1)	2·665(1)
Cu–L	2·177(8)	2·145(2)	2·185(3)	2·185(3)
Cu–O	1·980(7)	1·976(3)	1·973(3)	1·974(2)
C–O	1·246(2)	1·240(5)	1·249(4)	1·249(4)
Shift of Cu‡	0·207(3)§	0·231(2)	0·210(1)	0·226(1)
Cu–O–C	122·6(6)	122·6(3)	123·4(2)	121·4(2)
O–C–O	125·6(9)	128·4(4)	125·8(3)	127·8(3)
$-2J$§	326·0	489·0	333·0	507·0

† Bernard *et al.* (1979).
‡ The deviations of the Cu atoms from the O_4 plane.
§ Average value.

However, the structure analysis of the acetate was incomplete (R=0·10) owing to the disorder of the acetate groups. To sum up, these studies show that the formates have longer Cu–O bond lengths and shorter Cu–L bond lengths than the acetates and that there is little magnetostructural correlation in these dimeric copper(II) carboxylates. Furthermore, structures of the following dimeric copper(II) acetates and propionates were re-determined precisely at room temperature and at 120 K:

IX. $R=CH_3$, $L=H_2O$
X. $R=CH_3$, L=py
XI. $R=C_2H_5$, $L=H_2O$
XII. $R=C_2H_5$, L=py

by Uekusa *et al.* (1990).

The molecular structure of **IX** at 120 K is also included in figure 17. Table 6 lists the $-2J$ values. In crystals of **IX**, EPR measurement (Abe 1958) indicated that there exist three dimer molecules with different orientations in the unit cell. The direction of the Cu–Cu axes estimated from single-crystal EPR spectra agreed with the X-ray results. **XI** was found to exhibit orientational disorder of the C_2H_5 group, which prevents

Table 6. The values of $-2J(cm^{-1})$ for the dimeric complexes **IX** and **XII**.

	L=H_2O	L=py
R=CH_3	300	343
R=C_2H_5	327	340

Table 7. The average Cu–O and Cu–L distances in **IX–XII**.

		L=H_2O		L=py	
		299 K	120 K	299 K	120 K
R=CH_3	Cu–O	1·969(1)	1·969(1)	1·974(3)	1·970(1)
	Cu–L	2·154(2)	2·145(1)	2·191(2)	2·182(1)
R=C_2H_5	Cu–O	1·963(9)	1·970(5)	1·973(3)	1·974(2)
	Cu–L	2·162(9)	2·141(5)	2·173(2)	2·166(2)

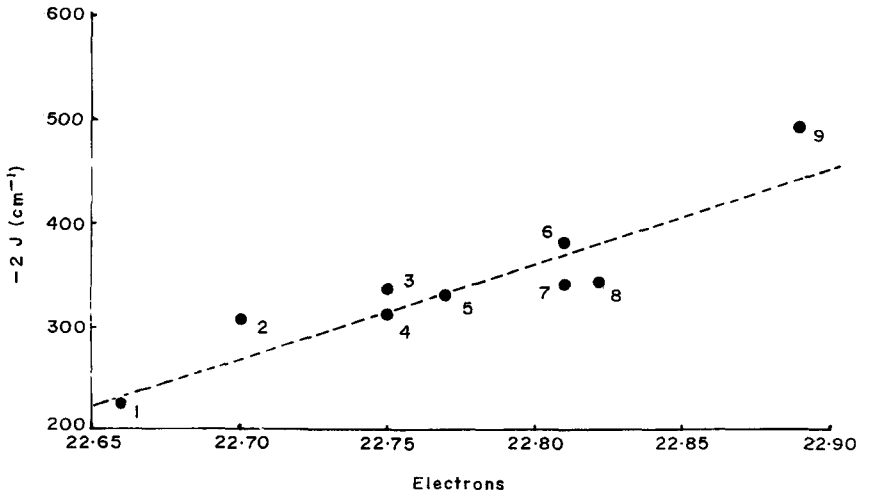

Figure 18. Values of $-2J$ are plotted against the total number of electrons in the bridging OCO group.

1. R=CCl_3 L=quinoline **2.** R=CCl_2H L=*p*-cyanotoluene
3. R=$CClH_2$ L=quinoline **4.** R=CF_3 L=benzonitrile
5. R=Ph L=pyridine **6.** R=$C(CH_3)_3$ L=quinoline, pyridine, α, γ-picoline
7. R=C_2H_5 L=pyridine **8.** R=CH_3 L=pyridine
9. R=H L=pyridine

references: **1**, **2**, **3**, **6**, **8**, **9**: Kato and Muto (1988), **4**: Melnik (1982), **5**, **7**: Tokii (private communication).

detailed comparison being made with the remaining three structures. Table 7 lists the Cu–O and Cu–L distances of the four complexes. As seen from table 7, it was again confirmed that there is little magnetostructural correlation in these copper(II) carboxylates. Then we are entitled to seek other properties that can correlate the magnetic character. An interesting empirical relation was found. In figure 18 the $-2J$ values of nine dimeric copper(II) carboxylates are plotted against the total number of electrons in the bridging O–C–O group (Yamanaka *et al.* 1990). The number of total electrons were calculated by molecular orbital methods. In principle, the total charge on the O–C–O group can be estimated by direct integration of the electron density or by electron-population analysis based on the observed structure amplitudes, however, the intensity data are still not accurate enough to give reliable results. The $-2J$ values appear to increase linearly with the number of electrons in the bridging group. The following observation also seems to support this inference. As seen from table 6, the $-2J$ value of $[Cu(CH_3COO)_2H_2O]$ is about $300\,cm^{-1}$. In the crystal of this complex, the molecules are strongly hydrogen bonded to the water molecules of the adjacent complex (O–H$\cdots$O = 2·86 Å). As a result, the charge density in the bridging OCO group is reduced by 0·014 *e*. If this charge by hydrogen bond formation is taken into account, the total number of electrons becomes 22·8. The plot of $[Cu(CH_3COO)_2H_2O]_2$ approaches the broken line illustrated in figure 18.

5. Dynamical structure analysis of crystalline state reaction

A very effective method elucidating the mechanism of a solid-state reaction may be to observe the crystal structures of several intermediate states as well as those of the reactant and the final product. This is not always easy to realize because the initiation of the reaction often occurs at defect or surface sites in the crystal and the crystal lattice is destroyed as the reaction proceeds; moreover, if the reaction proceeds too rapidly, intermediate structures cannot be determined by X-ray diffraction. In favourable cases, the solid-state reaction is known to proceed without degradation of crystallinity. Consequently, slow single crystal-to-single crystal transformation in the solid state is a very attractive system. If the structures at several intermediate stages are known in detail, it is possible to obtain a quantitative relationship between the macroscopic reaction rate and the microscopic atomic arrangement in the crystal. Such a stepwise X-ray structure determination is called 'dynamical structure analysis' (Ohashi 1988). A system suitable for dynamical structure analysis was found by chance during the comprehensive studies on asymmetric hydrogenation catalysed by cobaloxime complexes (Ohashi 1977). Cobaloxime is an abbreviation of *bis*(dimethylglyoximato)cobalt(III). During several structure analyses of cobaloxime complexes aimed at interpreting their catalytic capability for asymmetric hydrogenation, it was found that the chiral cyanoethyl (cn) group in a cobaloxime complex crystal is racemized by X-ray exposure without degradation of crystallinity. Figure 19 shows the reaction scheme (Ohashi *et al.* 1981)). In the figure [(R)-1-cyanoethyl][(S)-α-methylbenzylamine]cobaloxime is shown. Two molecules of dimethylglyoxime coordinate to the central cobalt atom through four nitrogen atoms to form a square-planar structure. A chiral organic amine and cyanoethyl group are bonded axially with respect to the coordination plane from opposite sides, completing a six-coordinate octahedral complex.

The chiral cn group is racemized by X-ray exposure without degradation of crystallinity. When this phenomenon was found in 1977, it was thought to be a rather

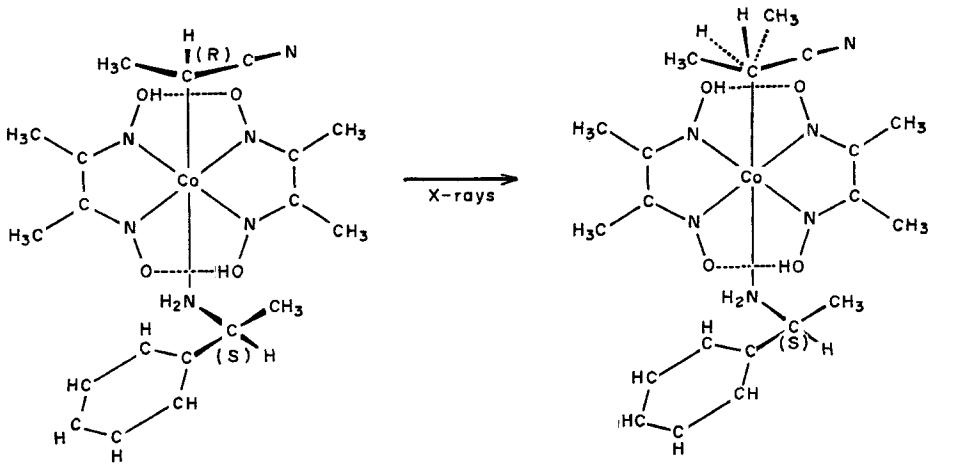

Figure 19. Racemization of the cn group in a crystal of [(R)-1-cyanoethyl][(S)-α-methylbenzylamine]*bis*(dimethylglyoximato)cobalt(III).

exceptional case of the solid-state reaction. Further studies, however, revealed that this new type of solid-state reaction occurs in a number of cobaloxime derivatives. Not only racemization, but also isomerization, were observed (Uchida *et al.* 1985).

5.1. *Direct observation of the crystalline state racemization*

The crystal composed of the molecule illustrated in figure 19 undergoes a change in unit cell dimensions without degradation of the lattice structure when exposed to X-rays. The monoclinic space group $P2_1$ stays unchanged. Figure 20 shows the change in the unit cell dimensions with irradiation time. The values of b, β and V increase, whereas those of a and c decrease with time. Approximate first-order reaction curves are obtained by least-squares fitting of the observed values, the rate constant being $3{\cdot}3 \times 10^{-6}\,s^{-1}$. If the irradiation is interrupted, the change in cell dimensions becomes undetectable and, when the irradiation is resumed, the change continues as before. The electron density at the stages A, B, C... F and G were calculated. Significant changes in electron density were observed only in the vicinity of the cn group. In figure 21 (*a*) are shown the composite electron-density maps of the cn group at the initial A stage, viewed along the normal to the average cobaloxime plane. Figure 21 (*b*) shows the composite difference density maps at the stage B. This is the difference between the electron-density maps of the A stage and those of the B stage. There appears a trough at the position of the methyl group and a peak appears in the vicinity of the methyl group. Figure 21 (*c*) shows the corresponding maps at stage F. The new peak grows higher and the trough becomes deeper. The position of the new peak corresponds approximately to that expected for the methyl substituent in the cn group when the absolute configuration of the cn group is inverted from R to S with the cyanogroup fixed. Figure 21 (*d*) shows the composite electron-density maps at the final stage G. Comparing figures 21 (*a*) and (*d*) one can easily realize that the cn group is becoming disordered at the final stage. Conversion of the asymmetric carbon atom of R configuration to S implies that one or more of the four bonds around the carbon atom, Co–C, NC–C, H_3C–C and H–C, are cleaved by X-irradiation in the transition state. EPR spectra

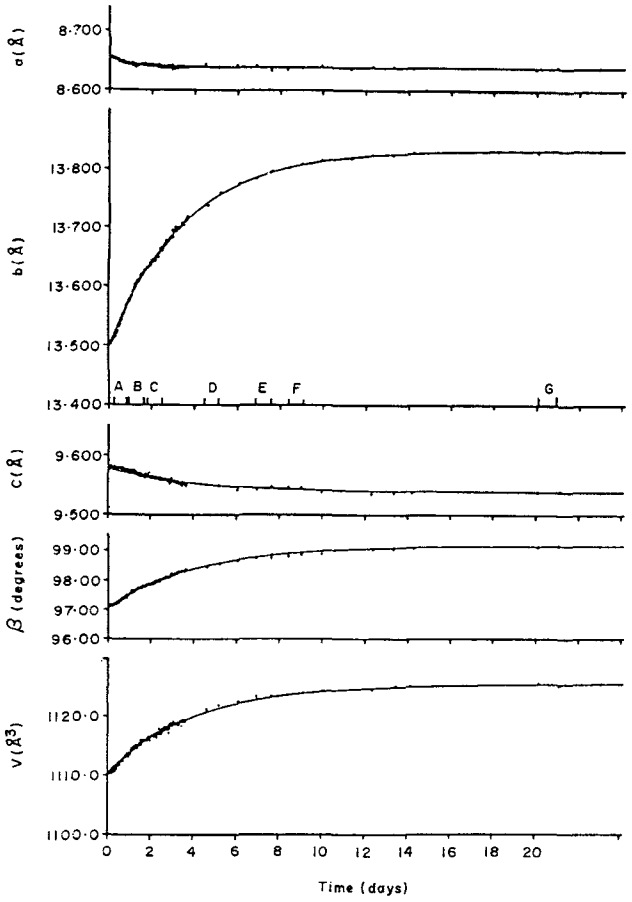

Figure 20. Change of the cell dimensions in the racemization. First-order kinetic curves were obtained by least-squares fitting.

measured after the irradiation of the crystals indicated that the Co–C bond was cleaved homolytically to produce the cn radical and the Co(II) complex (Gianotti *et al.* 1975). The Co–C bond dissociation energy has been determined to be 117–122 kJ mol^{-1} (Ohgo *et al.* 1986). The racemization rate of the complex by X-rays is far lower than that by visible light in the solid state and in an aqueous methanol solution (Ohashi *et al.* 1982). These observations may indicate that the secondary radiation produced from the Co atom may be responsible for the cleavage of the Co–C bond. This mode of racemization (figure 19) is called mode I.

A series of cobaloxime complex crystals were prepared with different bases as the second axial ligand, and whether or not the crystalline state racemization of the cn group occurs in different environments was examined. Table 8 lists the crystals. Structure analyses revealed that crystals of **1**–**7** have only one molecule per asymmetric unit. The space groups of the crystals are $P2_1$ or $P2_12_12$. In these crystals the complex molecules are arranged in such a way that each cn group is isolated with each other, thus each cn group is packed in the space formed by moieties other than the cn groups of the neighbouring molecules. Table 9 lists the reactivity of these crystals. Crystalline-state racemization occurs for the crystals of **1**, **2** (Ohashi *et al.* 1978) and **3** (Tamura

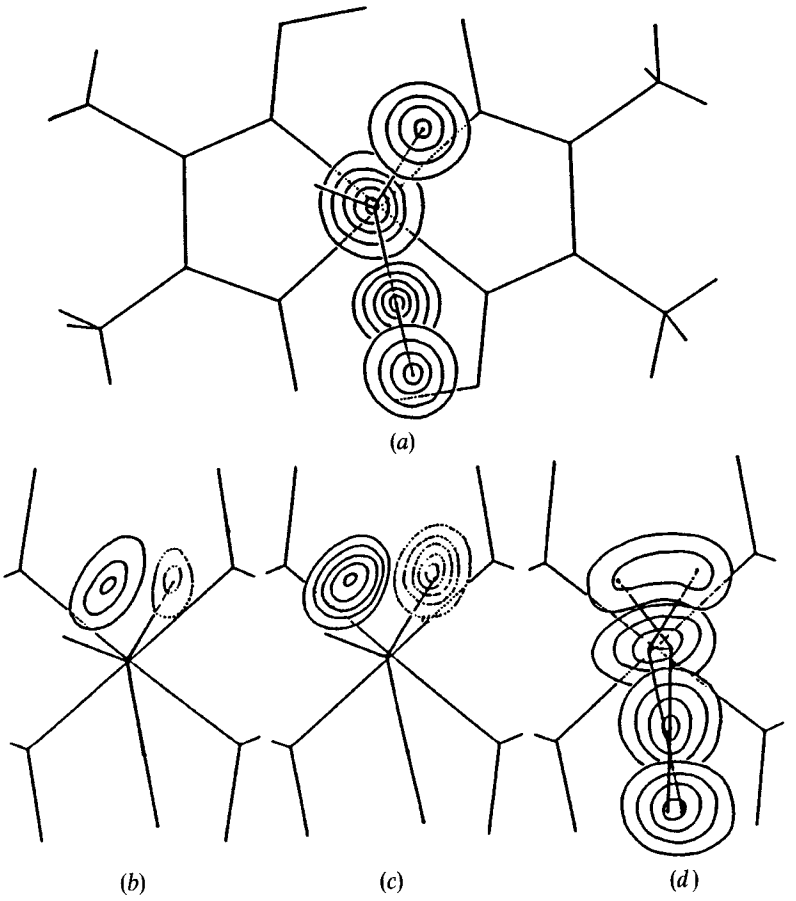

Figure 21. (*a*) Composite electron-density map of the cn group viewed along the normal to the cobaloxime plane at the initial stage. (*b*), (*c*) Composite difference maps at the B and F stages. (*d*) Composite electron-density map at the final stage. The contour interval is 1·0 e Å^{-3} in (*a*) and (*d*). In (*b*) and (*c*) the contour interval is 0·2 e Å^{-3}. The solid and dotted curves indicate positive and negative densities respectively.

Table 8. Crystals of cobaloxime complexes containing different axial base ligands: The first axial ligand is the cn group.

crystal	**1**	(S)-α-methylbenzylamine
crystal	**2**	(R)-α-methylbenzylamine
crystal	**3**	pyrrolidine
crystal	**4**	triphenylphosphine
crystal	**5**	tri-n-butylphosphine
crystal	**6**	diphenylethylphosphine
crystal	**7**	diethylphenylphosphine
crystal	**8**	pyridine
crystal	**9**	4-cyanopyridine
crystal	**10**	4-methylpyridine
crystal	**11**	diphenylmethylphosphine

Table 9. Rate constant and cavity volume of crystals **1**–**7** at 293*K*.

Crystal	Rate constant (10^{-6} s^{-1})	Cavity volume (Å^3)
1	3·06	14·53
2	2·10	12·23
3	1·69	11·55
4		11·31
5		10·64
6		10·18
7		8·40

1987) with different rates. Crystals of **4**, **5** (Kurihara *et al.* 1983a) **6** and **7** (Tomotake *et al.* 1984) are inactive at room temperature. Such differences in reactivity suggest that these differences are due to the different mode of packing in crystals. However, the density of the crystals ranges from 1·255 to 1·431 g cm^{-3} and does not seem to have any correlation with the reactivity. For instance, crystals of **5** have the lowest density, of 1·255 g cm^{-3}, and are inactive at room temperature. These observations suggest that the environment around the cn group, rather than the packing of the whole molecule, plays an important role in determining the reactivity. Consequently, the 'reaction cavity' is defined in order to represent the degree of packing around the reactive group. The reaction cavity is the concave space limited by the envelope surface of spheres whose centres are the positions of atoms surrounding the reactive group. The radius of each sphere is taken to be greater by 1·2 Å than the van der Waals radius of the corresponding atom. Thus the atomic centres of the reactive group can be considered to have access to any point in the cavity. The reaction cavity can be calculated on the basis of the crystal structure. Figure 22 shows a stereopair diagram of the reaction cavity for the cn group of crystal **1**. The calculated volumes of the reaction cavities for crystals **1**–**7** are listed in table 9. The reaction rate increases with increase in the volume of the reaction cavity. The volume necessary for the racemization to occur appears to be greater than 11·5 Å^{-3}. Thus the cavity size for the reactive group should be a good measure for this racemization.

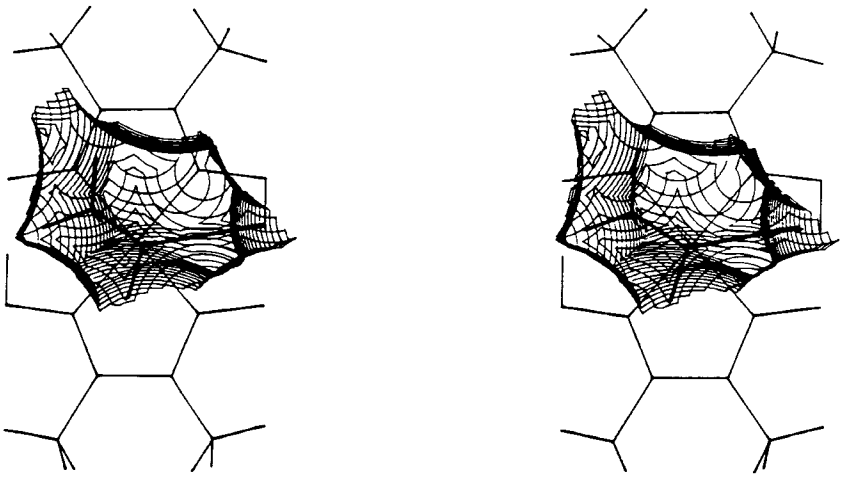

Figure 22. Stereoscopic drawing of the cavity for the cn group of crystal **1**. The contours are drawn in sections separated by 0·1 Å.

5.2. *Cooperative racemization of the two reactive groups (modes II and III)*

In crystals of **8**, **9** and **10** there are two molecules in an asymmetric unit. Figure 23 shows a projection of the crystal structures of **9** along the *a* axis at the initial stage (*a*) and the final stage (*b*) (Ohashi *et al.* 1983). In a non-centrosymmetric P1 cell of the initial structure, the two crystallographically independent molecules A and B are related by a pseudo-inversion centre except for the chiral cn group. After about 20 days of X-ray irradiation, only the cn group of the A molecule remains unchanged. Thus A and B molecules are related by a crystallographic centre of symmetry at the final stage. Hence the space group changes to $P\bar{1}$. This process is shown schematically in figure 24 (mode II). Such a mode of racemization, namely order-to-order racemization, was observed for **8** (Ohashi *et al.* 1982) and **10** (Uchida *et al.* 1984), accompanying the change of the space group from $P2_1$ to $P2_1/n$ and from $P2_1$ to $P2_1/a$ respectively. The crystal of **11** also undergoes racemization. At the initial stage two crystallographically independent molecules related by a pseudo-inversion symmetry becomes a crystallographic one at the final stage. This time, the space group changes from the non-centrosymmetric A2 to the centrosymmetric A2/a. At the final stage, the cn groups of the A and B molecules have disordered configuration (mode III, figure 24 (*b*)). Table 10 lists the volume of the reaction cavity and the reactivity of the crystals. The second mode is observed in the crystals of **8**, **9**, and **10**, in which only the cn group of the B molecule is fully inverted and a crystallographic inversion centre appears between the adjacent A and B molecules. The cavity for the A cn group is too small for the inversion of the A cn group, whereas the B cavity is significantly larger than the A cavity. The inversion causes closer molecular packing and the cell volume decreases. The driving force for this mode of racemization would be a decrease in enthalpy of the crystal. In the third mode (compound 11), both the A and B cn groups change to disordered racemates and a crystallographic inversion centre arises. The A and B cavities both have sufficiently large space for the inversion of the cn group. The greatest rate of racemization corresponds to the largest cavities.

A variety of slightly different modes of crystalline-state racemization has also been reported (Ohashi 1988, and references therein).

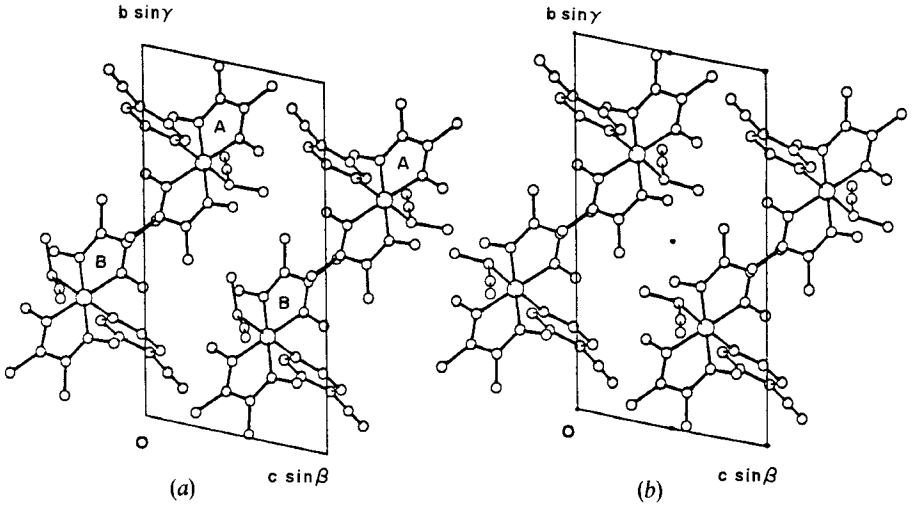

Figure 23. Crystal structure of **9** viewed along the *a* axis at the initial stage (*a*) and the final stage (*b*).

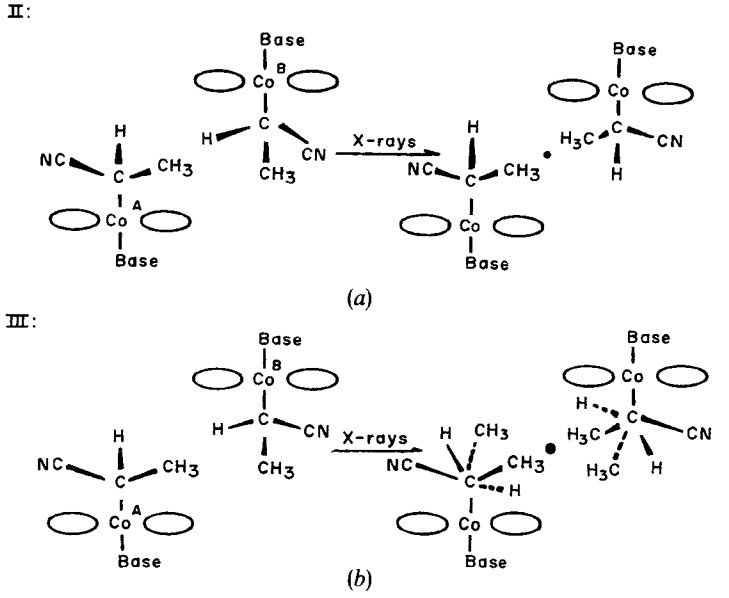

Figure 24. Schematic drawing of the racemization process of **9**((*a*), mode II) and **11**((*b*), mode III).

Table 10. Cavity volume and rate constants of crystals **8**–**11**.

		Cavity volume (Å^{-3})		Rate constant (10^{-6} s^{-1})	
Crystal	Mode	A	B	298 K	high temperature
8	II	8·89	11·34	2·86	50·6 (353 K)
9	II	7·97	10·37	1·56	
10	II	11·05	12·61	0·57	
11	III	17·08	18·01	4·81	5·07 (343 K)

5.3. *Multistage racemization*

Systematic studies on the crystalline-state reaction have been extended to the cobaloxime derivatives with bulkier methoxycarbonyl group with rotational freedom. This reactive group is hereafter abbreviated mce. Five cobaloxime derivatives involving mce, **12**–**16**, were synthesized and examined (figure 25).

Crystals of **12**, **13** and **16** did not exhibit the crystalline-state racemization at room temperatures. The crystals deteriorated on raising the temperature (Kurihara *et al.* 1984). Structural analysis of **12**, **13** and **16** revealed that each mce group fits so nicely in the respective cavity that the movement of the reactive species is suppressed. It was found that crystals of **14** contain solvent methanol and they lose the solvent molecules without degradation of crystallinity on exposure to X-rays at room temperature, where the unit cell volume contracts by about 5%. The rate of change was very rapid at the early stages but after 140 h it became slow and the structural analysis after desolvation could be successfully carried out. Figure 26(*a*) shows a projection of the crystal

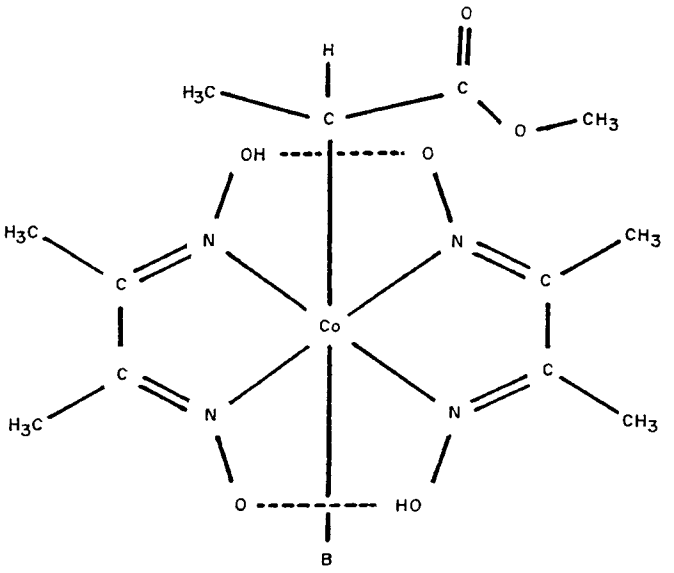

Figure 25. [(R)-1-ethoxycarbonylethyl]cobaloxime with a base ligand B, where B is **12** is (S)-α-methylbenzylamine; **13** is (R)-α-methylbenzylamine; **14** is pyridine; **15** is 4-chloropyridine; and **16** is 4-cyanopyridine.

structure of **14** at the initial stage (293 K). There are two molecules A and B in an asymmetric unit. The A and B molecules are related by a pseudo-centre of inversion except for the chiral mce groups. Figure 26 (*b*) illustrates the relative arrangement of the two mce groups of the A and B molecules. They are surrounded by the methanol molecules of crystallization. The conformation of the two mce differs: the methyl group and the carbonyl oxygen atom are *cis* in A, whereas they are in *trans* positions in B. The absolute configuration of the two mce group is R. Figure 27 (*a*) shows the crystal structure of **14** after the methanol molecules have been completely removed. The mce group of the B molecule rotates around the Co–C bond and fills up the void space formerly occupied by the methanol molecules. Nevertheless the R absolute configuration of the mce group is retained. When the temperature was raised to 343 K, crystalline state racemization occurred and the cell dimension began to vary again. After 180 h the change eventually stopped. Figure 27 (*b*) shows the structure of **14** after the racemization. The mce groups of the A and B molecules are more closely packed than those in the chiral intermediate structure, because the crystal contracts along the *b* axis and the volume of the unit cell contracts by 14 $Å^{-3}$. The pseudo-inversion centre between the A and B molecules changes to a crystallographic inversion centre. The space group changed from $P2_1$ to $P2_1/n$. The A and B mce groups both take disordered conformations and fill the void space after the loss of the solvent of crystallization. That is, one half of the mce group is related to the other by a mirror plane through AA′ and perpendicular to the plane of the paper. At the initial stage, the carbonyl oxygen atom and the methyl group are *trans* in the B mce group, whereas they are *cis* eventually. Namely, the *trans* conformation is converted to *cis* at the intermediate and final stages. Such *trans* and *cis* conformations of the two independent mce groups at the initial stage were also observed in the crystals of **15** (Kurihara *et al.* 1983b).

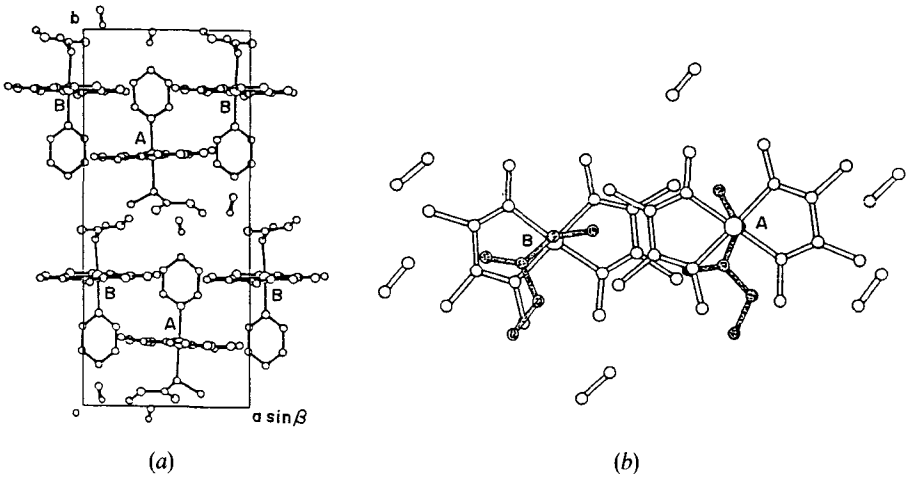

(*a*) (*b*)

Figure 26. (*a*) A projection of the crystal structure of **14** along the *c* axis at the initial state (293 K). (*b*) A part of the projection of the structure of **14** along the *b* axis, showing the relative arrangement of the A and B molecules.

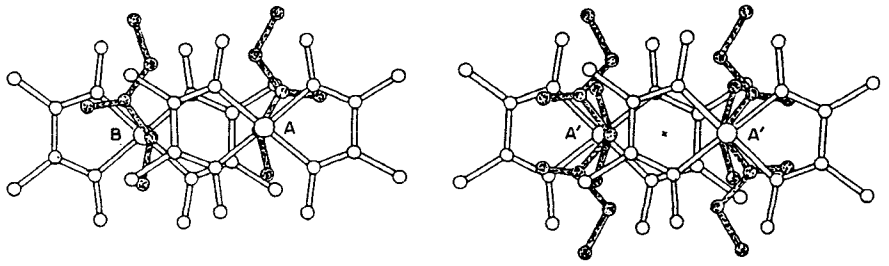

(*a*) (*b*)

Figure 27. (*a*) Arrangement of the A and B molecules in crystal **14** after the solvent molecules are completely removed. (*b*) The structure of (*a*) after the racemization.

5.4. *Reversible phase transition without degradation of crystallinity*

The β-cyano ethyl group (β-cn) bonded to the Co atom was found to transform to the α-cyanoethyl (simply abbreviated as cn) group in the cobaloxime complexes, when exposed to visible light in the microcrystalline state (Ohgo and Takeuchi 1985). Several crystals involving different base ligands were prepared and examined (Uchida *et al.* 1985, 1986, 1987). The crystals of (β-cyanoethyl) (4-methylpyridine)cobaloxime were found to undergo reversible phase transition at about 360 K without degradation of crystallinity (Uchida *et al.* 1988). Structural analyses of the high- and low-temperature phases revealed that the conformation of the β-cyanoethyl group changes on passing through the transition temperature. Figure 28 illustrates the conformational changes of the β-cn groups before and after transition, viewed along the normal to the cobaloxime plane. At 298 K there are two crystallographically independent molecules A and B in the unit cell. The orientation of the β-cn groups differs in A and B. Above the transition temperature the two conformations become the same by rotation of the group around

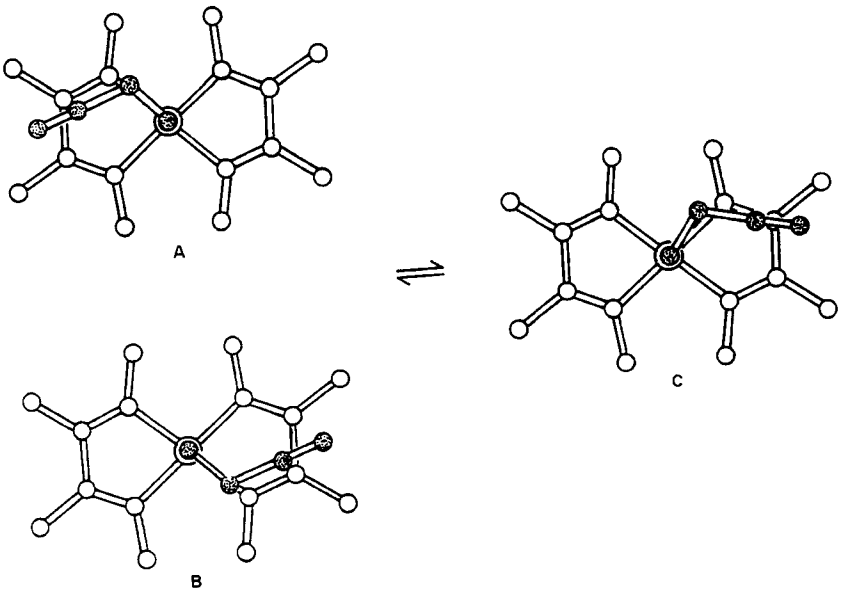

Figure 28. Conformation of the β-cn groups of the A, B and C molecules viewed along the normal to the cobaloxime plane.

the Co–C bond (C). The A and B β-cn groups are related to C by mirror planes through the short and long axes of the cobaloxime plane respectively. The mechanism of the transition without degradation of the crystallinity can be reasonably interpreted in terms of the cavity volumes for the A, B and C β-cn groups. They are considered to have the same volume at the transition temperature. Further studies on β-cyanoethyl cobaloxime complexes with different base ligands revealed that single crystal-to-single crystal β→α racemization occurs on exposure to visible light (Ohashi 1990).

6. Concluding remarks

Determination of electron-density distribution by X-ray diffraction provides overall information on the asphericity of the d electron distribution in a transition metal complex as well as on the redistribution of electrons on chemical bond formation. Experimental charge distribution can be compared with theoretical calculations, but the results are still qualitative. Efforts should be concentrated on obtaining highly accurate measurements of X-ray intensities and methods of deriving results in a meaningful way. If the electron-density distribution and the geometrical arrangement of the atomic nuclei in a complex are known, it is possible, at least in principle, to predict all its physical and chemical properties on the basis of quantum mechanics. The dynamical structure analysis of crystalline-state racemization has made it possible to observe various reaction pathways and to obtain a quantitative relationship between the macroscopic reaction rate and the microscopic atomic arrangement in the crystal from intermediate structure determination of a series of related crystals. However, the crystalline-state reactions are exceptional cases of solid-state reactions in general. The time required for the three-dimensional data collection should be shortened

considerably. It is hoped that a wide variety of intermediate structures will be determined soon by means of high-intensity X-ray sources and highly efficient detectors. Then the quantitative mechanisms will be proposed for solid-state reactions.

References

ABE, J., 1958, *J. phys. Soc.*, **13,** 987.

BERNARD, M. A., BOREL, M. M., BUSNOT, F., and LECLAIRE, A., 1979, *Rev. Chim. Miner.*, **16,** 124.

BLEANEY, B., and BOWERS, K. D., 1952, *Proc. R. Soc. London* A, **214,** 451.

BROWN, G. M., and CHIDAMBARAM, R., 1973, *Acta crystallogr.* B, **29,** 2393.

BROWN, I. L., MCDUGLE, W. G. JR, and KENT, L. G., 1970, *J. phys. Chem.*, **69,** 2101.

COPPENS, P., and HALL, M., 1982, *Electron Distributions and the Chemical Bond* (New York: Plenum).

DAWSON, B., 1967, *Proc. R. Soc. London* A, **298,** 255.

DOEDENS, R. J., 1976, *Prog. inorg. Chem.*, **21,** 209.

FORKESSON, B., and LARSSON, R., 1976, *Chem. scripta.*, **10,** 105.

GIANOTTI, C., MERLE, G., and BOLTON, J. R., 1975, *J. organometall. Chem.*, **99,** 145.

GOODGAME, D. M. L., HILL, N. J., MARSHAM, D. F., SKAPSKI, A. C., SMART, M. L., and TROUGHTON, P. G. H., 1969, *Chem. Commun.*, 629.

GUHA, B. C., 1951, *Proc. R. Soc. London* A, **206,** 353.

HANSEN, N. K., and COPPENS, P., 1978, *Acta crystallogr.* A, **34,** 909.

HAY, P. J., THIBEAULT, J. C., and HOFFMANN, R., 1975, *J. Am. chem. Soc.*, **97,** 4884.

HIRSHFELD, F. L., 1977, *Israeli J. Chem.*, **16,** 226.

ISHIGURO, T., ISHIZUKA, N., MIZUTANI, N., KATO, M., TANAKA, K., and MARUMO, F., 1983, *Acta crystallogr.* B, **39,** 564.

ITO, K., NAKAMURA, D., KURITA, Y., ITO, K., and KUBO, M., 1961, *J. Am. chem. Soc.*, **83,** 4526.

IWATA, M., and SAITO, Y., 1973, *Acta crystallogr.* B, **29,** 822.

JOHANSEN, H., 1976, *Acta crystallogr.* A, **32,** 353.

JOHNSON, C. K., 1965, *ORTEP*, Report ORNL-3794, Oak Ridge National Laboratory, Tennessee, U.S.A.

JOTHAM, R. W., KETTLE, S. F. A., and MARKS, J. A., 1972, *J. chem. Soc. Dalton Trans.*, 428.

KADOTA, S., YAMADA, I., YONEYAMA, S., and HIRAKAWA, K., 1967, *J. phys. Soc. Japan*, **23,** 751.

KANAMORI, J., 1960, *J. appl. Phys.*, **31,** suppl. 14S.

KATO, M., JONASSEN, H. B., and HANNING, J. C., 1964, *Chem. Rev.*, **64,** 99.

KATO, M., and MUTO, Y., 1988, *Coord. Chem. Rev.*, **92,** 45.

KIJIMA, N., TANAKA, K., and MARUMO, F., 1981, *Acta crystallogr.* B, **37,** 545; 1983, *Ibid.* B, **39,** 557.

KISHITA, M., INOUE, M., and KUBO, M., 1964, *Inorg. Chem.*, **3,** 237.

KURIHARA, T., OHASHI, Y., SASADA, Y., and OHGO, Y., 1983b, *Acta crystallogr.* B, **39,** 243.

KURIHARA, T., UCHIDA, A., OHASHI, Y., SASADA, Y., OHGO, Y., and BABA, S., 1983a, *Acta crystallogr.* B, **39,** 431.

KURIHARA, T., UCHIDA, A., OHASHI, Y., SASADA, Y., and OHGO, Y., 1984, *J. Am. chem. Soc.*, **106,** 5718.

LARSSON, R., and FORKESSON, B., 1977, *Chem. Scripta.*, **11,** 5.

MARRAM, E. P., MCNIFF, E. J., and RAGLE, J. L., 1963, *J. phys. Chem.*, **67,** 1719.

MARUMO, F., ISOBE, M., and AKIMOTO, S., 1977, *Acta crystallogr.* B, **33,** 713.

MELNIK, M., 1982, *Coord. Chem. Rev.*, **42,** 259.

MIYATA, N., TANAKA, K., and MARUMO, F., 1983, *Acta crystallogr.* B, **39,** 561.

MORELAND, J. A., and DOEDENS, R. J., 1978, *Inorg. Chem.*, **17,** 674.

NAKAMURA, D., KURITA, Y., ITO, K., and KUBO, M., 1960, *J. Am. chem. Soc.*, **82,** 5783.

OHASHI, Y., 1977, *J. Crystallogr. Soc. Japan*, **19,** 303 (in Japanese); 1988, *Acc. Chem. Res.*, **21,** 268; 1990, *Molec. Cryst. liq. Cryst.* (to be published).

OHASHI, Y., SASADA, Y., and OHGO, Y., 1978, *Chem. Lett.*, 743.

OHASHI, Y., UCHIDA, A., SASADA, Y., and OHGO, Y., 1983, *Acta crystallogr.* B, **39,** 54.

OHASHI, Y., YANAGI, K., KURIHARA, T., SASADA, Y., and OHGO, Y., 1981, *J. Am. chem. Soc.*, **103,** 5805; 1982, *Ibid.*, **104,** 6353.

OHBA, S., TORIUMI, K., SATO, S., and SAITO, Y., 1978, *Acta crystallogr.* B, **34,** 3535.

OHGO, Y., ORISAKU, K., HASEGAWA, E., and TAKEUCHI, S., 1986, *Chem. Lett.*, **27.**

OHGO, Y., TAKEUCHI, S., 1985, *J. chem. Soc. chem. Commun.*, 21.

OKAZAKI, A., 1969a, *J. phys. Soc. Japan*, **26,** 870; 1969b, *Ibid.*, **27,** 518.
OKAZAKI, A., and SUEMUNE, Y., 1961, *J. phys. Soc. Japan*, **16,** 176.
ORGEL, L. E., 1966, *An Introduction to Transition Metal Chemistry, Ligand-Field Theory*, Second edition (London: Methuen).
ROGERS, D. B., SHANNON, R. D., PREITT, C. T., and GILLON, J. L., 1971, *Inorg. Chem.*, **10,** 723.
SAITO, Y., 1979, *Inorganic Molecular Dissymmetry* (Berlin: Springer Verlag), pp. 89–115.
STEWART, R. F., 1969, *J. chem. Phys.*, **51,** 4569.
TAKAZAWA, H., OHBA, S., and SAITO, Y., 1988, *Acta crystallogr.* B, **44,** 580; 1990, *Ibid.* (to be published).
TAMURA, T., 1987, Master's Thesis, Tokyo Institute of Technology.
TANAKA, K., 1988, *Acta crystallogr.* A, **44,** 1002.
TANAKA, K., KONISHI, M., and MARUMO, F., 1979, *Acta crystallogr.* B, **53,** 1303.
TANAKA, K., and MARUMO, F., 1982, *Acta crystallogr.* B, **38,** 1422; 1990 (to be published).
TOMOTAKE, Y. UCHIDA, A., OHASHI, Y., SASADA, Y., OHGO, Y., and BABA, S., 1984, *Acta crystallogr.* B, **40,** 1684.
TORIUMI, K., and SAITO, Y., 1983, *Advances inorg. Chem. Radiochem.*, **27,** 28.
UCHIDA, A., DANNO, M., SASADA, Y., and OHASHI, Y., 1987, *Acta crystallogr.* B, **43,** 528.
UCHIDA, A., OHASHI, Y., and SASADA, Y., 1986, *Nature*, **320,** 51.
UCHIDA, A., OHASHI, Y., SASADA, Y., and OHGO, Y., 1985, *Acta crystallogr.* C, **41,** 25.
UCHIDA, A., OHASHI, Y., SASADA, Y., OHGO, Y., and BABA, S., *Acta crystallogr.* B, **40,** 473.
UCHIDA, A., SASADA, Y., and OHASHI, Y., 1988, *Acta crystallogr.* B, **44,** 249.
UEKUSA, H., OHBA, S., and SAITO, Y., 1989, *Acta crystallogr.* C, **45,** 377.
UEKUSA, H., OHBA, S., SAITO, Y., SUZUKI, I., KATO, M., TOKII, T., MUTO, Y., and BÉNARD, M., 1990 (to be published).
VAN NIEKERK, J. N., and SCHOENING, F. K. L., 1953, *Acta crystallogr.*, **6,** 227.
WILLIS, B. T. M., 1969, *Acta crystallogr.* A, **25,** 277.
YAMANAKA, M., UEKUSA, H., OHBA, S., SAITO, Y., IWATA, S., KATO, M., TOKII, T., and MUTO, M., 1990, *Acta crystallogr.* C (to be published).
YAWNEY, D. B. W., and DOEDENS, R. J., 1970, *Inorg. Chem.*, **9,** 1626.